Master Erasmus Mundus in
Color in Informatics and Media Technology (CIMET)


# Image Texture, Uniformity, Homogenity and Radiation Dose Properties in CT

Master Thesis Report

Presented by

Dawid Mozejko

and defended at

Gjøvik University College

Academic Supervisor(s): Marius Pedersen, Dag Waaler
Anne Catrine Martinsen, Hilde K. Andersen

Jury Committee: Rafael Huertas Roa
Olivier Alata

# Image Texture, Uniformity, Homogenity and Radiation Dose Properties in CT

Dawid Mozejko

2013/07/15

# Abstract

In medical imaging, especially when potentially harmful X-ray radiation is used to obtain diagnostic data, it is important to reduce the risk the patient is exposed to. For that reason it is expected to obtain maximum diagnostic information with minimum exposure to harmful factors, by accurate selection of scanning parameters. This thesis analyzes the noise properties of two CT scanners, GE Lightspeed HD 750, and Toshiba Aquillion ONE, based on reported differences in appearance of the images scanned. Catphan Phantom 600 uniformity module is scanned with both scanners, using range of configurations and extension rings simulating patients of different sizes. 60 datasets were obtained and analyzed in terms of the uniformity, homogeneity, noise texture and spectral power distribution. The results show that GE scanner provides images less contaminated with noise when larger patient is scanned or the scanned region is enveloped with big volumes of matter or high density regions, that are sources of artifacts in CT. On the other hand, it is Toshiba that performed better when desired region of scanning was easily accessable (small or slim patients). Because human body is a source of many artifacts that increase the difficulties of obtaining desired data, it is understandable, that medical practitioners have more success in retriving diagnostically important information from images from GE scanner, which has better results in similar simulated conditions.

# Preface

I would like to express my gratitude to Marius Pedersen and Dag Waaler from Gjovik University College, who both supported me constantly with their experience, opinion and ideas. I am also very grateful to Anne Catrine Martinsen and Hilde Kjernlie Andersen from Oslo University Hospital, for their elasticity in thesis topic design, constant support and introducing me to hospital equipment and personnel. This thesis would suffer in quality if it wasn't for these people. I am very thankful for their cooperation and support. Finally, I would thank my beloved Kasia for her patience during these two years and not giving up on us.

# Contents

# List of Figures

# List of Tables

# 1 Introduction

Computed Tomography (CT) is a very widely used medical imaging technique used for diagnostic purposes. CT usage around the world is increasing rapidly in last decades. [1, 2] CT uses X-rays penetrating the body of the patient, to create the image. Absorbed high energy photons in the X-rays can increase chances of cancer for the patient. CT X-ray dose is highest among medical radiography techniques. [3] Because of that, and the popularity of CT, use of lowest possible dose that provides satisfactory diagnostic information is vital for patients safety. [4] However, different vendors design scanners and image reconstruction methods to create the image in their own way, which results in different images for scanners from different vendors, even if the parameters and objective is the same.

The motivation for this thesis is to compare image quality for different reconstruction methods and different CT scanners. As new CT scanners are introduced in a radiological department of the hospital, optimizing the image quality is challenging due to the fact that the image texture is different for new scanners compared to the older scanners. Also, new reconstruction methods are introduced without much information about the functionality, so it might be difficult to choose which type of reconstruction kernel is the most advantageous for one specific examination. Some radiologists are complaining about the image quality for the newest CT scanners, even though the vendors claims that the image quality is the best on the market. The aim of this thesis is to compare the image quality and image texture for two different CT scanners, and to objectively evaluate if there are differences in the image quality, or the complains are due to personal preference, or radiologists becoming acustomed to specific vendor. This can be schematically shown on the Figure 1.

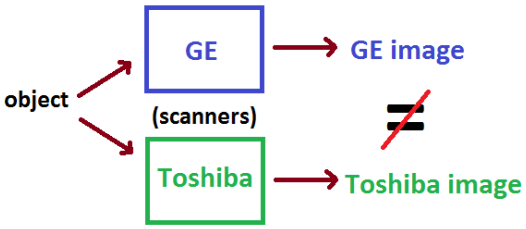


Figure 1: This figure schematically represents the research question of the thesis. If an object is measured with two scanners, with the same parameters designed for obtaining the same particular kind of diagnostic information, the results supposed to be the same, or very similar. However, this is not the case. This hypothesis, based on the reports of medical personel, must be evaluated.

It is important to lower the dose, but perhaps a good step would be also to take full advantage of the options already available. Namely, the correct protocol and scanner selection, and setting up parameters that give maximum information with minimal radiation dose applied. Patients

receiving CT scans are of all ages and what follows, sizes. However, the predicted radiation dose received by patient is calculated for 'standard patient', and thus, larger patients receive lower radiation dose, while thinner patients - higher.

This thesis is structured in the following way. In the Background chapter, the principles of functioning of the CT imaging is explained, as well as common types of artifacts that affect the quality of the images. Finally, the mathematical foundations of the tools used for analysis of the scanned datasets are explained. In the Methodology, the parameters of the CT scanners used in the research are detailed, as well as the characteristic of the phantom which was the scanned object. Furthermore, the details and motivation for specific analysis and comparison of the datasets that were acquired through scanning the phantom are explained. In the Results chapter, the outcomes of the dataset analysis are described, while Discussion chapter sums up these findings and their meanings. Variety of other experiments and analysis that could be performed for better understanding the issues and results are mentioned in the chapter Future Work.

# 2 Background

In this chapter, the basic principles and physical phenomena connected with CT were explained. It also contains mathematical explanation of techniques used in the data analysis.

## 2.1 Technical concepts of X-ray Computed Tomography

This section focuses on how the information is being obtained and processed to create the final image in CT.

### 2.1.1 Principles of functioning

Most important elements of CT scanner are x-ray tube and detector array, which are mounted on rotating circular system, which allows scanning and obtaining information about the scanned body from every angle. Data for the final image is obtained by measuring attenuation of radiation on the path from X-ray tube, which generates the X-rays, through the object, to the detector. It is schematically presented in Figure 2. The attenuation profile obtained this way is not an universal value independend from scanning parameters, because it depends on the spectral energy of x-ray tube used. Due to that, a term *CT number* has been introduced, to give the value in relation to the attenuation coefficient of water. The unit of CT number is Hunsfield Unit (HU). The equation for CT number is the following:

$$\text{CT value} = \frac{(\mu_T - \mu_{water})}{\mu_{water}} \cdot 1000 \text{ HU} \tag{2.1}$$

Relating the CT number to the water attenuation coefficient makes the values independent of scanning parameters, and makes it possible to establish expectable values for certain tissues. Examples of CT numbers can be seen in Table 1.

Table 1: Example approximate CT numbers of human tissues.

| tissue | CT number [HU] |
|---|---|
| bone | 1000 |
| muscle | 50 |
| blood | 20 |
| water | 0 |
| fat | -100 |
| lungs | -200 |
| air | -1000 |

### 2.1.2 Scanning modes

The X-ray tube and detector matrix are being rotated around the object, creating numerous projections, which was depicted in Figure 2. The image is usually created through so called

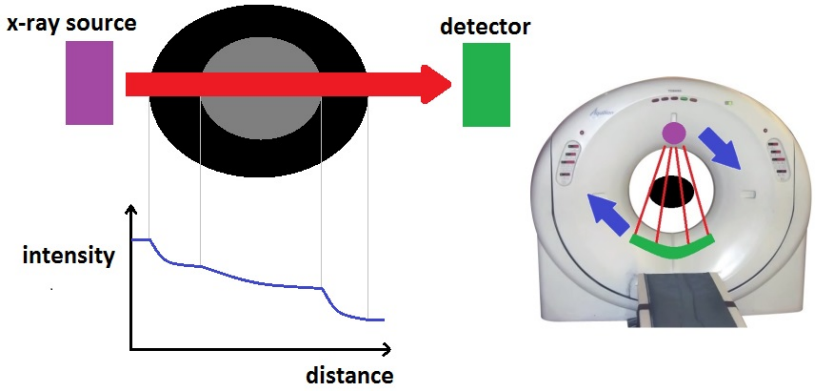


Figure 2: On the left, the schematic presentation of the X-ray beam attenuation is presented. If we assume that circular object has higher density where darker region is, then the X-ray beam will attenuate more while passing through it. This can be seen in the corresponding plot, under the schematic. On the right, general view on the scanner with symbolic addition of x-ray tube, body and detector matrix added.

covolution-backprojection procedure. In this procedure, each attenuation profile (projection) contributes to the pixel value in the final image at the location it corresponds to, but to the entire image as well. This way, blurring the final image occurs. To prevent this the convolution process is applied. The convolution of signal with a filter gives an opportunity to modulate it, and this way emphasize certain features, for example, bones. Several types of these *convolution kernels*, or *filters*, are in use, depending on the application. It can be noise suppressing for general body scans or edge enhancing for diagnosis of lung or liver pathologies. Figure 3 present schematic effect of convolution.

It is important to realize that exact details of image reconstruction process are kept private by the scanner manufacturer. The end user receives the indications which reconstruction filter is recommended for specific applications. Such indications, without comparable numerical description, creates difficulties in choice of best fitted protocol to extract desired data.

## 2.2 Image Quality

A very important factor in CT is the radiation dose delivered to the patient during the scan. First of all, it is prefered to use the minimum dose necessary for a sufficient quality scan that provides information to give an accurate diagnosis. It can be said, that with higher dose, the image quality improves, because dose is inversely related to the magnitude of noise. Radiation dose is expressed as Computed Tomography Dose Index (CTDI) [1, 5]. The SI (International System of Units) unit of CTDI is Gray (Gy). CTDI can differ from absorbed dose, if patient size is not taken into account, because it expresses radiation per unit mass. [5] This way, CTDI of 20 mGy calculated for patient of standard body size, can be effectively even 40 mGy if the actual patient is a child. [5] Many details on managing patient dose is described in the document Managing Patient Dose in Multi-Detector Computed Tomography (32/219/06 Dec vers).

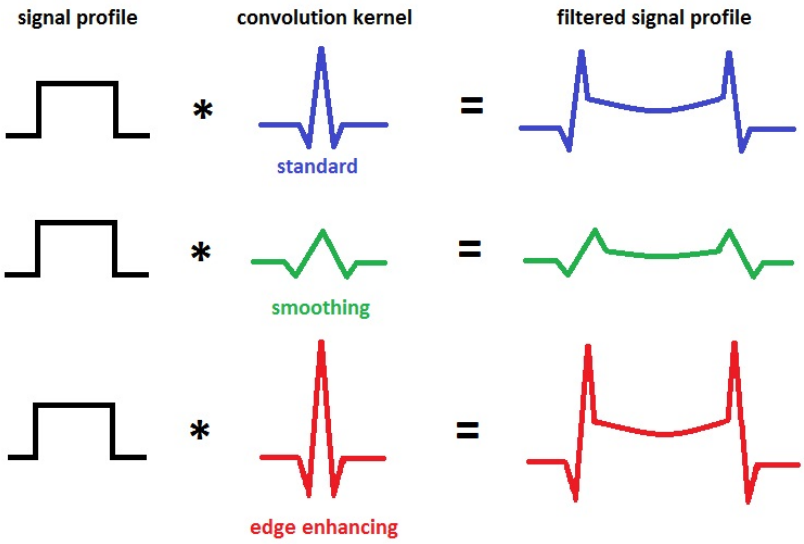


Figure 3: Figure presents effects of filtering the signal with three sample types of convolution kernels.

### 2.2.1 Artifacts

Infidelities in representation of the scanned object structure are called artifacts. It might be difficult to accurately determine which parts of an image are artifacts. In practical cases, where patient scans are analyzed, it depends mainly on the experience of the examiner. It is also important to understand the characteristic of artifacts of certain scanner or protocol. Two types of artifacts most prominent in the experiment are described in more details. First corresponds to so called beam hardening effect. [1, 6] It can be seen as darker (less dense) regions between more dense regions. In real cases it is most prominent around thick bone structures. The origin of this artifact is due to broad spectrum of radiation attenuates differently. The main factors are radiation energy together with object size and density. Mean energy of the spectrum increases when thick or dense structures are encountered. As a result, attenuation profiles can give inconsistent pixel values, dependent on the projection direction. This effect can be observed in the right part of Figure 4 , as darker regions inside the phantom, suggesting that there are differences in density within the phantom, which is not the case. In ideal case, this should be visualized as uniform region, similarly to image on the left of the figure. The beam hardening effect, and thus differences between those two scans, come from different volume that the x-rays have to penetrate. Related to this is the problem of streaking artifacts, visible as darker shadow of the most dense regions. It is caused by photono starvation - many X-ray photons are absorbed by high density medium and this way too few of them provide the information about the regions behind those of high density [1, 6]

Another prominent artifact observable in Figure 4 is exceeding the limits of field of measurement. This happens when part of patient/object is inside the scanner gantry, but outside the field of measurement. This leads to hyperdense regions depicted on the border of the field of view. This artifact is present in this experiment for the largest ring case, which is 550mm in major

axis, while maximum field of view that could be used was 500mm. Artifacts often stack making dealing with them difficult at times. However the development in scanning technology reduces this problem in modern scanners.

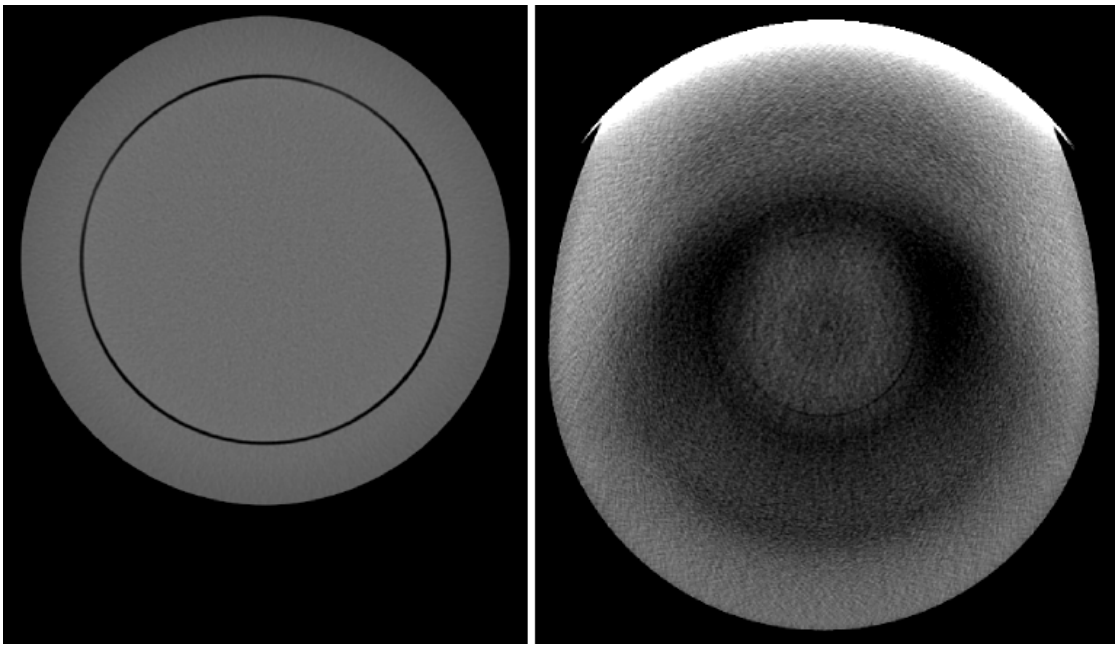

Figure 4: The left part presents the CT scan of the phantom, while the right part is the phantom with extension ring. White half-circle on top is an artifact corresponding to region where extension ring exceeded the field of measurement. Dark regions inside are due to beam hardening effect.

## 2.3 Mathematical Analysis

Because the idea of the thesis is to find a method and compare properties of different scanners and scanning protocols used, certain methods were used for mathematical analysis of the data. A2part from mean pixel values, and standard deviation across chosen regions, the Noise Power Spectra were calculated. With the resultant data, the image quality and certain noise parameters could be assesed. [7]

### 2.3.1 Noise Power Spectrum

Noise Power Spectrum (NPS) is the noise power frequency-wise. The NPS characterizes both the magnitude and spatial frequency distribution of image noise [8, 9] The level of randomness at specific spatial frequencies is described by magnitude of the NPS, while the shape shows the concentration of noise power in freqnuency space. As can be seen in Figure 5,uniform image disturbed with red noise, which is mainly low-frequency noise, has mottled appearance, while finer grains resulting from blue noise, have high-frequency power. [10] Note that the figure represents 1 dimensional NPS, where the spatial information is lost.

With spectral and spatial characteristic included, the NPS can provide much more information

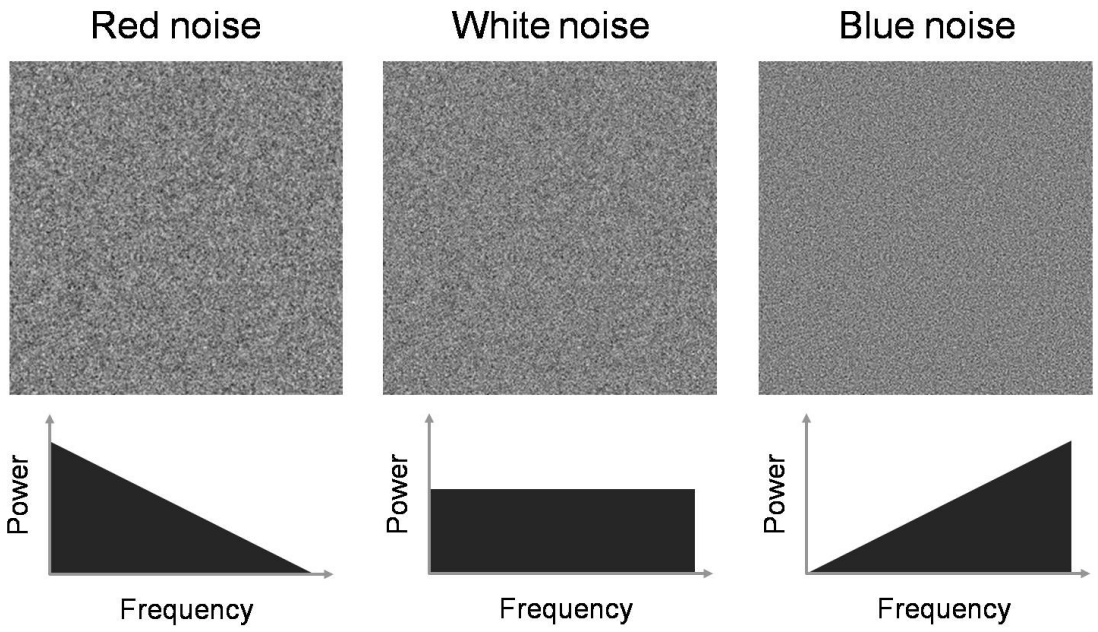


Figure 5: Example noisy image(top) and corresponding noise power spectra(bottom).

than standard deviation, and was chosen for the main tool in this experiment. The formula for NPS is the following:

$$\mathrm{NPS}(u,v) = \frac{d_x d_y}{N_x N_y} \cdot |F\left[I\left(x,y\right) - P\right]|^2 \tag{2.2}$$

where $u$ and $v$ are spatial frequency $[mm^{-1}]$ in directions $x$ and $y$. $F$ represents two dimensional Fourier Transform, *I(x,y)* contains CT number at pixel location (x,y). P is the mean pixel value across whole ROI, and is subtracted from each pixel to remove dc component, and reduce artifacts such as dark current, beam hardening, and x-ray scattering. [11]

Due to the image reconstruction process that filters the signal in specific manner, the NPS of CT image can be described with a bandpass filter. Such information is available in CT scanner manuals from different vendors.

### 2.3.2 Statistical analysis tools

In order to compare the NPS between the datasets, the Root Mean Square Difference [12] (RMSD) was calculated. It is expressed with the following equation:

$$\mathrm{RMSD} = \sqrt{\frac{1}{N}\sum_{i=1}^{N}\left(D_1 - D_2\right)^2} \tag{2.3}$$

where N is the number of samples, $D_1$ and $D_2$ are first dataset, and the dataset compared to it, respectively. RMSD equal zero means that two datasets are equal. Higher the RMSD, the dataset $D_2$ differs from dataset $D_1$.

# 3 Methodology

## 3.1 Equipment and setup

To evaluate the differences between the scanners, it was decided to perform series of scans with different parameters that provide a wide spectrum of comparison. For several reasons, the experiment was not conducted on real patients. First of all, radiation exposure for humans should be limited to situations when it is absolutely necessary. Patient movement, and the movement of their organs would cause errors in the data, that would deny repeatability of the scans. Because all these reasons, a phantom, an artificial cylindrical structure roughly resembling human body, was used as an object for scanning. It is a common practice in research on CT, and for periodic calibration of scanners in hospitals.

The experiments were conducted on two CT scanners, first was GE Lightspeed HD 750, and second was Toshiba Aquillion ONE. For short, they will be reffered as GE and Toshiba, respectively.

On these scanners, images of a Catphan 600 phantom from The Phantom Laboratory were taken [13]. This phantom can be seen in Figure 6, where it is mounted on wooden case stand. The Catphan 600 phantom is divided into modules, and in this study the CTP486 image uniformity module was used. This module is made of an uniform material, that it designed to have a CT number in the range of 20HU of that of water when using standard protocols. [14] This module can be used to measure the spatial uniformity, texture, or noise values.

On top of that, additional antropomorphic annuli (later reffered to as rings) were mounted on the phantom, to simulate patients of different sizes. Four cases were investigated, one without an additional ring, and three with rings of different sizes. These rings were of oval shape, with following dimensions:

1. **CTP579** - 25-35cm oval OD uniformity material body annulus
2. **CTP651** - 30-38cm oval OD uniformity material body annulus
3. **CTP599** - 45-55cm oval OD uniformity material body annulus

The radiographic density was controlled with mAs value in the way to obtain desired CTDI. Measurements were conducted with three different CTDI of approximately 10, 15 and 20 mGy.

Although an attempt was made to measure the data for two different slice thicknesses, 2.5 and 5 milimeters, only 5 milimeters thickness were used in the analysis, due to differences in the setup and protocols between GE and Toshiba.

GE datasets consisted of 8 slices, but to avoid risk of border slices falling outside the uniformity module and being corrupted, 4 central slices were used in both GE and Toshiba. It means, each dataset with specific parameters, consisted of 4 slices, where each was a matrix 512x512 pixels. These were then processed according to the need of analysis.

List of all settings and parameters used for scanning are listed in Table 2. In the end, this

Figure 6: Photo showing the Catphan 600 phantom.

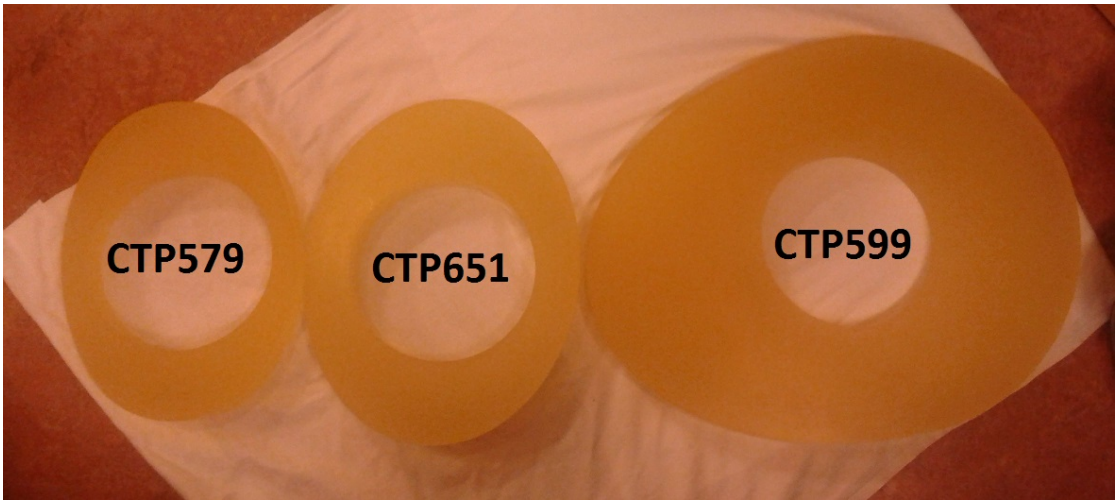


Figure 7: Photo showing the relative size of the rings used in experiment.

choice of measurements and parameters gives an opportunity to compare the corresponding reconstruction kernels of different scanners, keeping the other parameters the same.

Table 2: Scan settings used in experiment. All scans were done in axial mode.

| scanner | GE Discovery CT750 HD | Toshiba Aquilion One |
|---|---|---|
| kVp | 120 | 120 |
| CTDI [mGy] | 10, 15, 20 | 10, 15, 20 |
| reconstructed FOV [mm] | 210, 360, 400, 500 | 210, 360, 400, 500 |
| slice thickness [mm] | 5 | 5 |
| number of slices | 4 | 4 |
| image matrix size [pix] | 512x512 | 512x512 |
| convolution kernels | STANDARD, LUNG | FC08, FC18, FC56 |

For sake of simplicity, a coding system was introduced to name the dataset and parameters used during acquisition. It carries information about which scanner was used, which ring(if any) was used, which reconstruction filter was used, and what dose was used. Figure 8 presents the details of the coding system used, with all possibilities.

## 3.2 Analysis of uniformity across the module

Since the noise is the main interest, Regions Of Interest (ROIs) were determined from the scans, to perform analysis on. It was selected the way that the area of ROI consists of uniform central region of the phantom, so that areas outside of uniformity module are not disturbing the results.

This section gives details on all types of data analysis and comparisons performed, the motivation and methodology for that. It should be noted, that use of rings introduce a problem of decreased number of pixels that compose the ROI. As mentioned before, single slice in all cases was 512x512 matrix. However, the displayed field of view(DFOV) was changing, with addition of rings. This is an effect of following relation: $\mathrm{pixel\,size} = \frac{\mathrm{DFOV}}{\mathrm{matrix\,size}}$ . As a result, the size of a single pixel was increasing with the rings, but the dimensions of ROI in milimeters were kept possibly constant. The complete presentation of this can be seen in Table 3

Table 3: This table presents how the FOV changes with introduction of rings, and what effects it has on pixel size of ROIs, if area of ROI is preserved

| | FOV[mm] | [pixels/mm] | ROI size [pixels] | ROI size [mm] |
|---|---|---|---|---|
| no ring | 210 | 2.44 | 25.00 | 10.25 |
| 1st ring | 360 | 1.42 | 15.00 | 10.55 |
| 2nd ring | 400 | 1.28 | 13.00 | 10.16 |
| 3rd ring | 500 | 1.02 | 11.00 | 10.74 |

Part of quality control in CT, and main use of CTP486 image uniformity module of Catphan 600, is to measure the mean CT number in selected ROIs, to examine the uniformity across the module. It is particulary interesting when rings are included, because they influence the beam hardening effect.

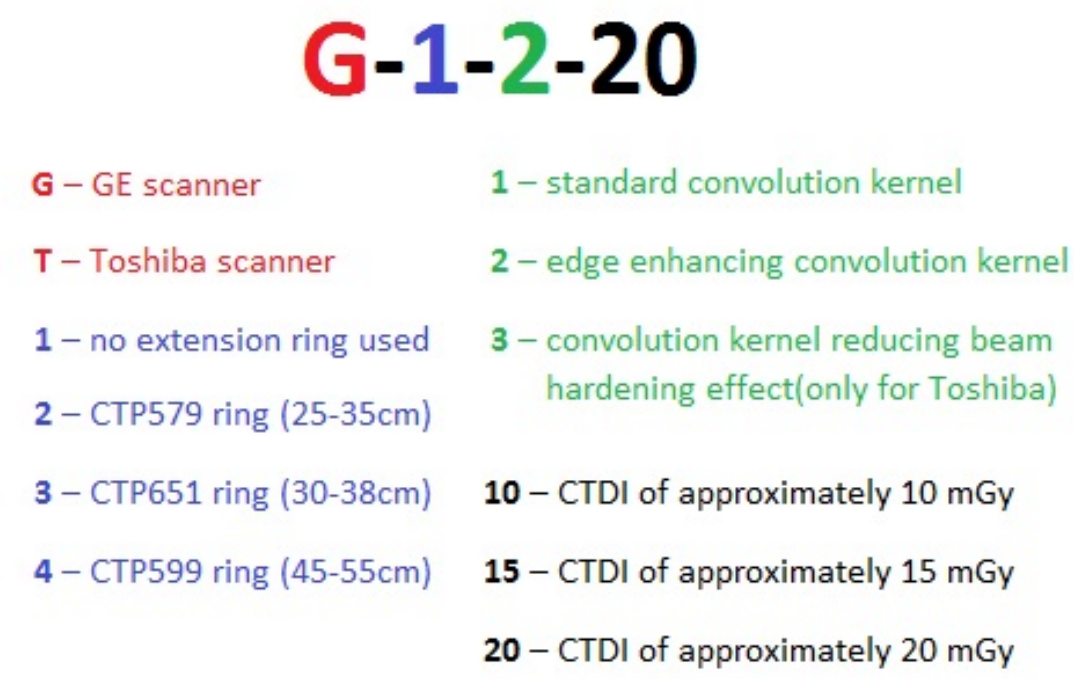


Figure 8: Presentation of dataset coding system. In the example , G-1-2-20 indicates a dataset obtained on the GE scanner, without an additional ring, with the edge enhancing convolution kernel, and with CTDI of 20 mGy.

The datasets were analyzed in Matlab in the following manner: 5 ROIs were selected as visible on Figure 9. Each ROI consisted of data of such region selected in each slice of dataset. For each ROI, mean value and standard deviation was calculated, for comparison of uniformity across the phantom.

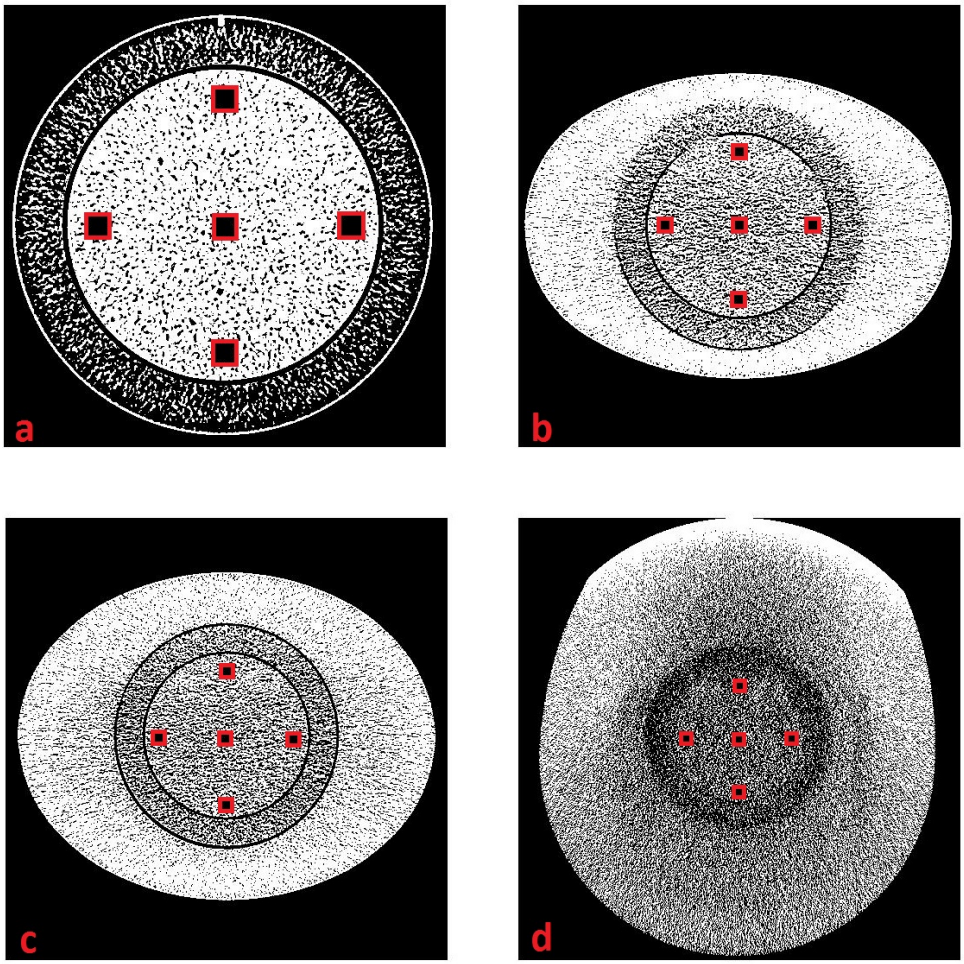


Figure 9: Red bordered squares present the ROI used for uniformity analysis. Although the real size in milimeters is similar, size of single pixel increases with the field of view. Number of data pixels contributing to those ROIs is biggest when no ring is used **(a)**, and decreases with ring CTP579 **(b)**, CTP651 , and is the smallest for biggest ring, CTP599 **(d)**. Note that ring CTP599 dimensions exceeds the maximum field of view of the scanner.

## 3.3 Noise Power Spectrum analysis

The calculation of NPS of given image slice results in a 2 dimensional NPS. Such presentation is not convinient for quantitative analysis of numerous datasets, and is often converted to 1

dimensional NPS, with use of techniques like radial averaging. [11] An example of such NPS extraction can be seen in Figure 10.

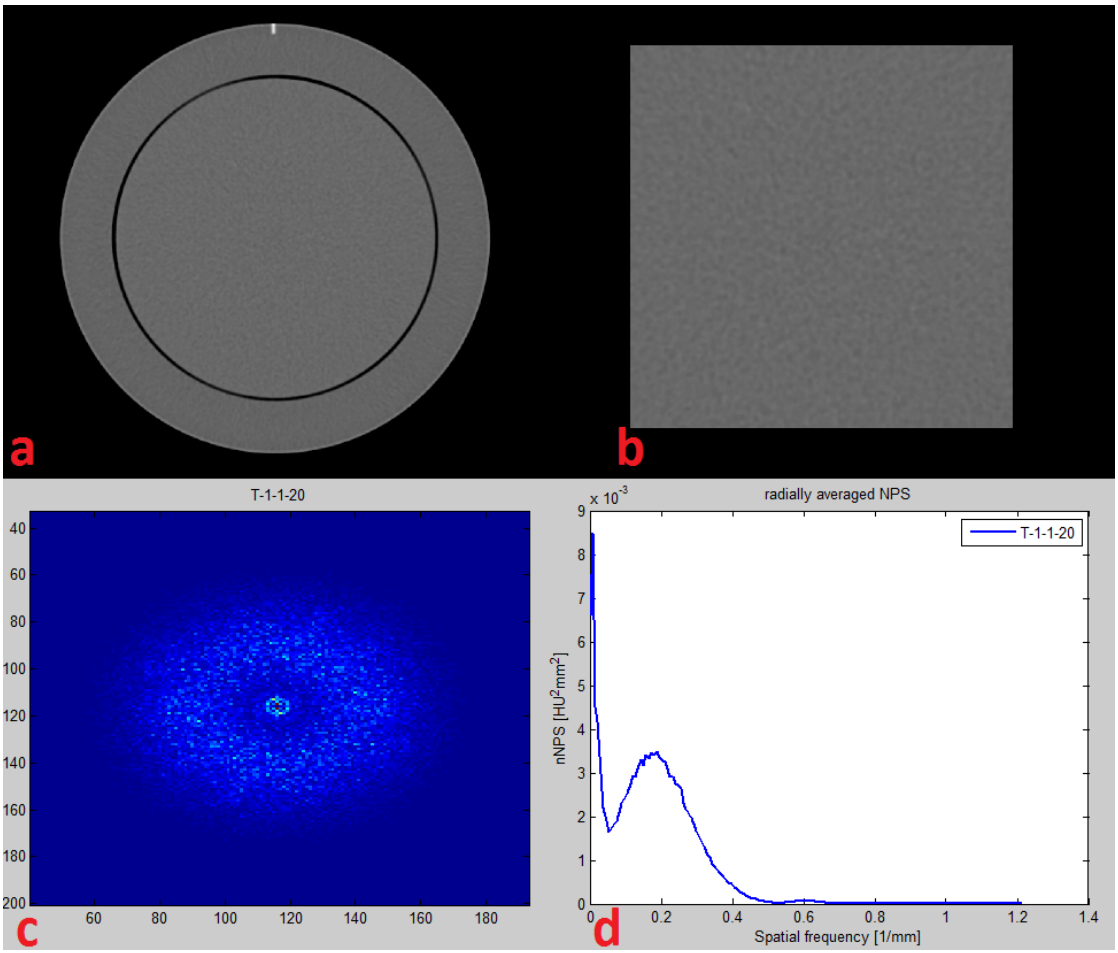


Figure 10: Scanned image of the phantom **(a)**, ROI extracted from the image for NPS calculation **(b)**, 2D NPS calculated from ROI **(c)**, NPS radially averaged for 1D display **(d)**.

For NPS analysis, introduction of rings decrease the amount of pixels in ROI used for NPS calculation. These differences can be seen in Table 4. This has negative effect on NPS analysis, as less points result in less smooth NPS. However, it is inevitable, since constant dimensions of 512x512 pixel images were obtained. Figure 11 presents this effect in a schematic way.

Two cases of NPS were analyzed, apart from one described in the Background section, an attempt to remove the systemic noise was made. In order to achieve that, the NPS was calculated in following way; first, the NPS of each slice was taken, and these 4 Noise Power Spectra were averaged, resulting in averaged NPS of the dataset. Secondly, the data of all 4 slices were averaged, creating average slice. This slice, has strenghtened intensity in regions of similar intensity across all contributing slices, so non-stochastic. When the NPS of such an average slice is obtained it consists of spectrum of noise that was present in all slices, which suggest that it is

Table 4: This table present the changes of ROI area with introduction of rings over the phantom. It can be seen, that with additional rings, less pixels can be used for NPS analysis.

| | FOV[mm] | [pixels/mm] | limit [pixels] | ROI size [pixels] | Pixel size [mm] | ROI size [mm] |
|---|---|---|---|---|---|---|
| no ring | 210 | 2.44 | 243.8 | 230 | 0.41 | 94.34 |
| 1st ring | 360 | 1.42 | 142.2 | 130 | 0.70 | 91.41 |
| 2nd ring | 400 | 1.28 | 128.0 | 116 | 0.78 | 90.63 |
| 3rd ring | 500 | 1.02 | 102.4 | 90 | 0.98 | 87.89 |

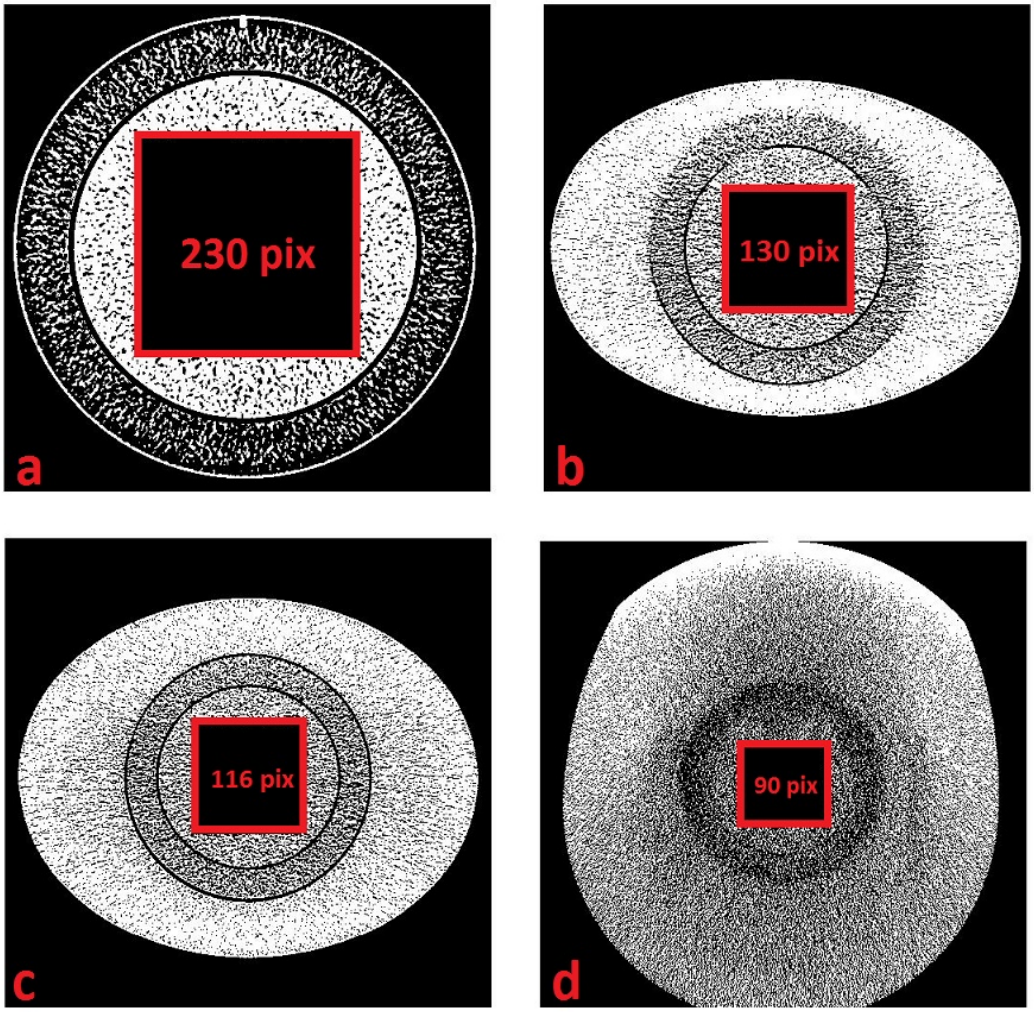


Figure 11: Red border squares present the ROI used for NPS analysis. Although the real size in milimeters is similar, number of data pixels contributing to those ROIs is biggest when no ring is used **(a)**, and decreases with ring CTP579 **(b)**, CTP651 **(b)**, and is the smallest for biggest ring, CTP599 **(d)**. Note that ring CTP599 dimensions exceeds the maximum field of view of the scanner.

deterministic, and its source is in the flaws of hardware or reconstruction kernel.

Following, the obtained 2 dimensional NPS was normalized by dividing by the area of ROI. In the end, the NPS was radially averaged to provide possibility to compare the shapes of the spectra of NPS. However, it must be noted that only the datasets where no extension ring was used were spatially symmetrical. For those with rings attached that was not the case, due to ellipsoid shape of the ring. Because the datasets were compared within the ring used, which then had similar spatial distribution of NPS, and due to decreasing number of pixels within ROI, with increasing size of ring(this can be seen in Table 4) it was decided to continue with radial averaging to preserve sufficient amount of data for averaging and obtaining smooth curves. With the largest ring, where size of ROI is 90x90 pixels, a different method of representing 1D NPS, like averaging from line/few lines of pixels would provide very little information. Although it is common in literature to use few ROIs from each slice [11, 15, 8] , it was decided not to follow this habit, again for the sake of smoothness of the NPS of phantom with added rings. With such division, the resultant NPS has less samples, and usually, more noise. This becomes more visible and problematic with rings attached, since the number of samples decreases either way.

### 3.3.1 Filtering with Human Visual Response Function

Since the question of the thesis is connected with human perception, it is interesting to filter the obtained NPS with the human visual response function, to evaluate which differences between the vendors/kernels may be perceived by an observer. Vision research has clearly demonstrated that the capacity to detect and identify spatial form varies widely as a function of target size, contrast, and spatial orientation. Since the conditions on investigating the CT images varies a lot in the hospital considered (practicioners can view images at any place around the hospital), the parameters for the human visual response function were taken from literature. [11, 16] The equation is designed for luminance human visual response function, as the CT scans are usually not displayed in color.

$$\rho = r \cdot \frac{FOV \cdot R \cdot \pi}{D \cdot 180} \tag{3.1}$$

$$V(\rho) = \left| \eta \rho^{\alpha_1} \cdot e^{-\alpha_2 \rho^{\alpha_3}} \right|^2 \tag{3.2}$$

where $\rho$ is the radial spatial frequency (cycles/degree) as seen by an observer, r is spatial frequency in $[mm_1]$, FOV is the reconstructed field of view [mm], R is the viewing distance [mm], D is the size of the displayed image [mm], $\eta$ is a factor to normalize V ($\rho$) to one at its maximum value, and parameters (a1, a2, a3) are (1.5, 0.98, 0.68). $\rho$ must be calculated first, to make both NPS and human visual response function functions of spatial frequency in $[mm_1]$. This way the filtering can be performed.

In Figure 12 the change of human visual response function for different rings can be seen. It can be seen that this function changes with the rings. This is happening due to different FOV used for different rings, and FOV is a parameter of the equation for human visual response function. With larger FOV, the sensitivity is shifted towards lower frequencies.

These curves are point-by-point multiplied with 1D NPS to obtain filtered NPS. The resultant curve presents all the noise of the ROI that is visible for human observer when looking at the image. This fact opens another option of comparing the NPS, which will be described in the

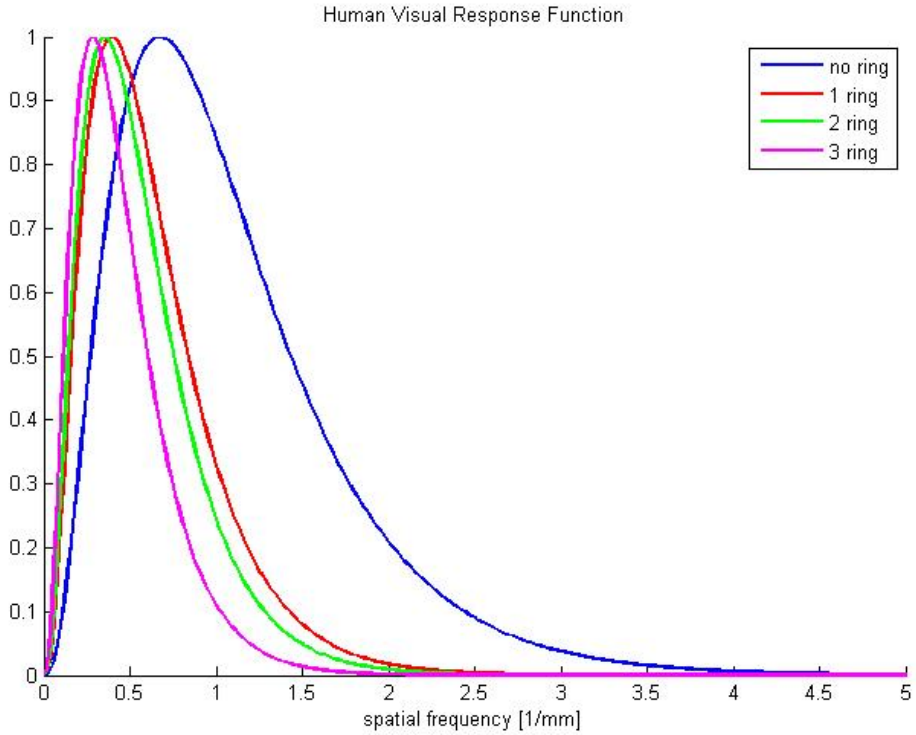


Figure 12: The shape of human visual response function for viewing distance of 40cm and display size of 30cm. The size of reconstructed image varies with the ring used, and thus affects the shape of the function.

following subsection.

### 3.3.2 Root Mean Square Difference and Total Visible Noise

After obtaining filtered NPS, RMSD was calculated for the datasets. Because RMSD calculates difference between two different sets of samples, it was decided to compare Toshiba results to GE. In other words, higher the RMSD, the more different Toshiba datasets are from GE datasets (and vice versa). They were compared in the following way, Toshiba datasets with convolution kernels FC18 and FC08 (standard and standard compensating for beam hardening effect) against GE standard, and Toshiba FC56 (edge enhancing convolution kernel) against GE lung (edge enhancing). Also, they were all compared with the same radiation dose, and extension ring. This way, the only parameter that differed, was the scanner producer and its design of convolution kernel, which has theoretically the same application.

Apart from that, the filtered NPS presenting total visible noise, gives an opportunity to compare datasets against how much noise that affects the observer they contain. This is the information that could be directly related to the impression that the observer has about the quality of the image, and his/her ability to see the diagnostically significant features. Because the comparison of numerous curves simultaneously limits the perspective, it was decided to use the area covered under these curves, as the number representing Total Visible Noise (TVN). TVN gives simple, one-value information about the amount of the noise in the dataset, and was used to order the datasets.

# 4 Results

## 4.1 Analysis of uniformity across the module

Figure 13 presents the numeration of ROIs on the simplified drawing of central uniformity module of phantom. Values of ROIs were compared in the manner that ROI 1 (top), 3 (central) and 5 (bottom) were showing the uniformity change in vertical direction, while ROIs 2 (left), 3 (central) and 4 (right) represented the changes in uniformity in horizontal direction. [14]

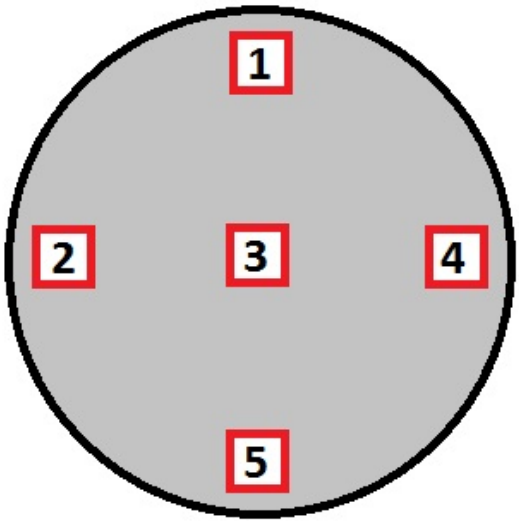


Figure 13: Schematic representation of ROIs numbering.

This order of comparison was used because it was expected that central ROI value will differ from the border ones. Such difference would come from the fact that central ROI is further on the path of X-rays than the border ones. This way the beam hardening effect is more influential, and decreases the final CT number in the center. For the case without any ring, these differences will be minimal, and this is supported by the results. In Figure 14 one can see that apart from G-1-1-10 and G-1-2-10 (lowest radiation dose among plotted datasets), all datasets have lowest CT number in the center of the uniformity module. The complete table with values for all the ROIs in all datasets can be found in Appendix B.

When the ring is included, these differences become more visible, and is most prominent along the major axis of the ring. In 85% of all datasets, the central ROI has the lowest mean CT number from ROIs on the major axis of ellipse(This means ROI number 2, 3 and 4 for first and second ring, ROIs number 1, 3 and 5 for largest ring. For datasets where no ring was used,

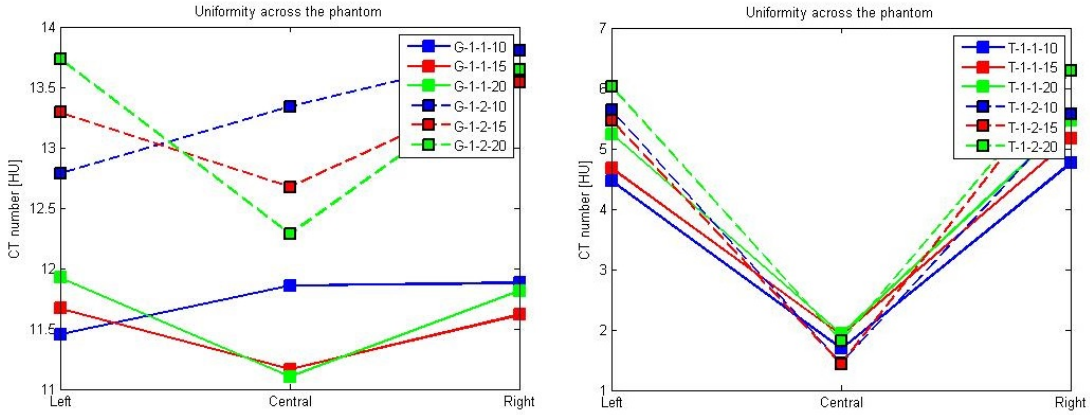


Figure 14: Uniformity of GE(left) and Toshiba(right) standard and edge enhancing kernels, for different radiation doses.

central ROI number 3 must have had the lowest mean CT number of all five ROIs). In Figure 15 the evaluation whether the central ROI has the lowest mean CT number or not is presented. Boxplot was used for that because it is a more accurate method than plain comparison of mean values. It can be stated with 95% confidence, that central ROI has the lowest values from all three ROIs of the dataset, if the notches of the border ROIs (2 and 4) do not overlap with notches corresponding to the central ROI. [17]

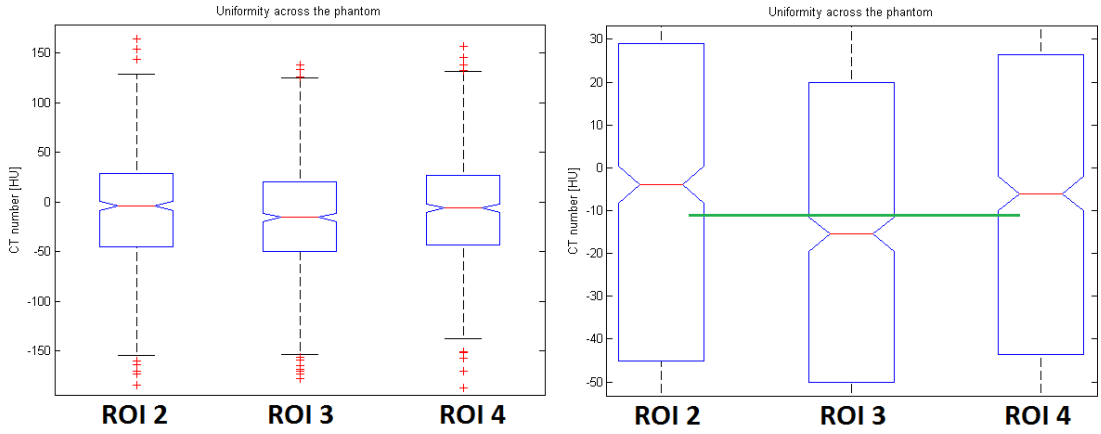


Figure 15: On the left, the boxplot of a dataset with the ring mounted on was chosen for an example analysis. The plot on the right is just a magnification of the left hand side plot, and in addition a green horizontal line is drawn for easier verification that the notches do not overlap at all. This example boxplot was created for dataset T-3-1-20.

On top of that, in 67% of datasets, the central ROI has the highest standard deviation from all ROIs, which indicate that the magnitude of the noise is the highest there. These statistics

show that beam hardening effect creates significant differences in the image in the theoretically uniform region of the phantom.

## 4.2 Noise Power Spectrum analysis

This is the main part of the information obtained from the data, and the most important results in terms of answering the research question, about the validity of the perceived difference, and character of the noise between GE and Toshiba scanners. Different spatial distribution of the NPS between different rings enforces comparisons of NPS between the datasets with the same FOV (same ring attached or no ring).

### 4.2.1 Effect of the dose on Noise Power Spectrum

The effect of dose change is well analyzed in the literature [**?**] , and will be recreated in here in one example for each convolution kernel. As can be seen in Figures 16 and 17, increase of the dose decrease the NPS magnitude. This can be also observed in Appendix B Table 2, where the standard deviation values of the datasets are given. The change of NPS magnitude with change of dose is very similar for both vendors and both standard and sharp kernels. The location of the peak does not change with the change of the dose. There are total 20 groups of datasets, where each group use exactly same parameters, except being in three different radiation doses (CTDI) cases. For all of them, the same effect was observed.

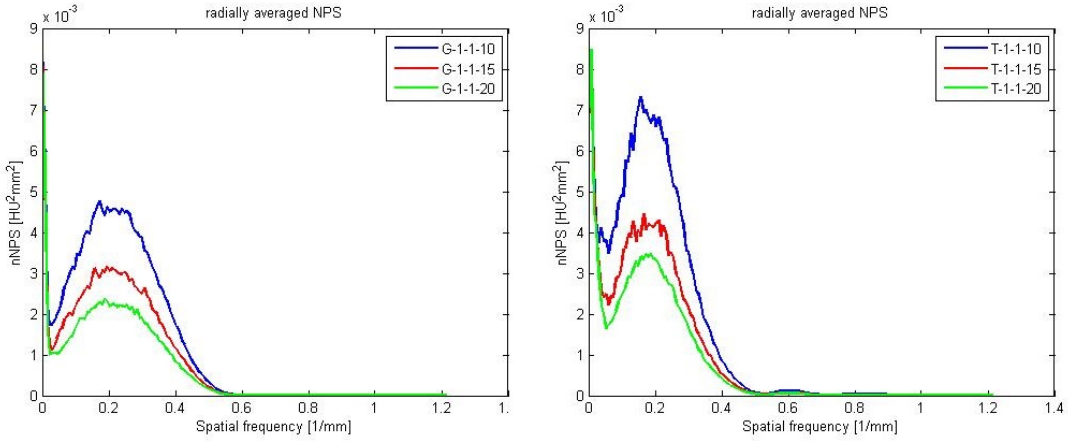


Figure 16: NPS of GE(left) and Toshiba(right) standard convolution kernel, for different radiation dose.

### 4.2.2 Comparison of different protocols and rings

In this subsection the GE and Toshiba kernels for no extra ring are compared, as well as the effect of adding rings for Toshiba. GE cannot be compared with Toshiba for the phantom with rings, because of enormous low frequency spike that makes any comparison impossible, due to its large magnitude in comparison to the rest of the NPS. This low-frequency noise is beyond human perception, and the reasons for its presence are only speculations.

Due to large magnitude difference between the NPS of edge enhancing and standard convolu-

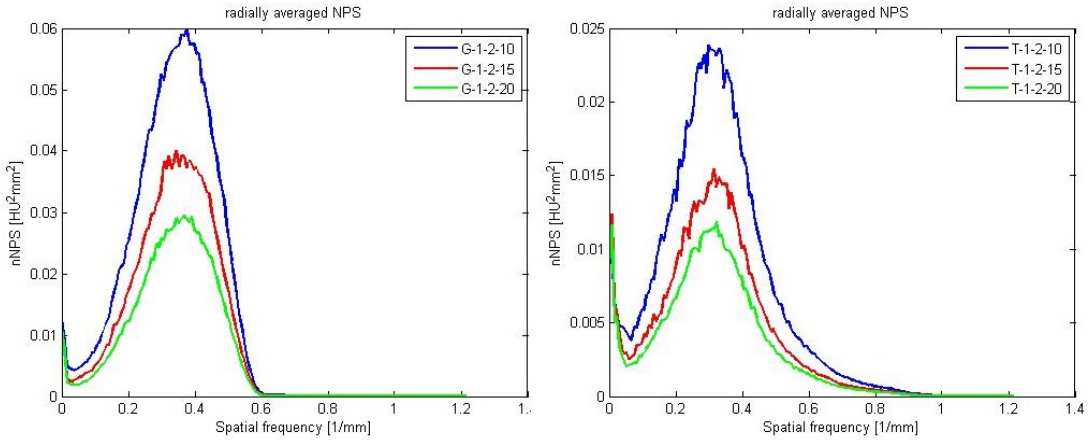


Figure 17: NPS of GE (left) and Toshiba (right) edge enhancing convolution kernel, for different radiation dose.

tion kernels, additional plot presenting the same data, but divided by area under the curve(instead of area of region of interest) is presented on the right from original plot. This way, the difference in shape and peak location can be seen, while the plot on the left informs about magnitude differences.

As can be observed on Figure 18, the NPS is slightly shifted towards higher frequencies for GE in comparison with Toshiba. Also, edge enhancing convolution kernels exhibit the same shift, in relation to standard kernels.

The same effects are present for Toshiba kernels with addition of rings(Figures 19 and 20) , sharper kernel NPS occupies longer frequencies, and has higher magnitude than standard one. It is particularly interesting that although the magnitude of NPS varies with different rings, the frequency of the peak is relatively constant. This means that rings contribute mostly to the magnitude of NPS, not changing the character of the noise. However, with increase of the noise magnitude, particular noise frequencies become more noticeable. Notice that there is about 10 times noise magnitude increase from datasets without to first ring, and from second to third ring. It can be also seen that the location of the peak does not change significantly.

Overall, from no ring to third ring, the magnitude increases almost 1000 times, while the FOV increases from 210mm to 500mm. This indicates that Toshiba scanner is very sensitive to the size of the object scanned. In the next subsection these results are compared with those for GE scanner.

### 4.2.3 Filtering with Human Visual Response Function

Comparison of the effect of the filtering the NPS with human visual response function gives an unique opportunity for Toshiba and GE kernels to be matched, due to elimination of huge low-frequency noise spike present in the GE NPS. This is a particularly vital comparison, because it helps answering the research question, whether the reported CT images differences are related to actual, physical differences of the output images, or the preference and confidence with the

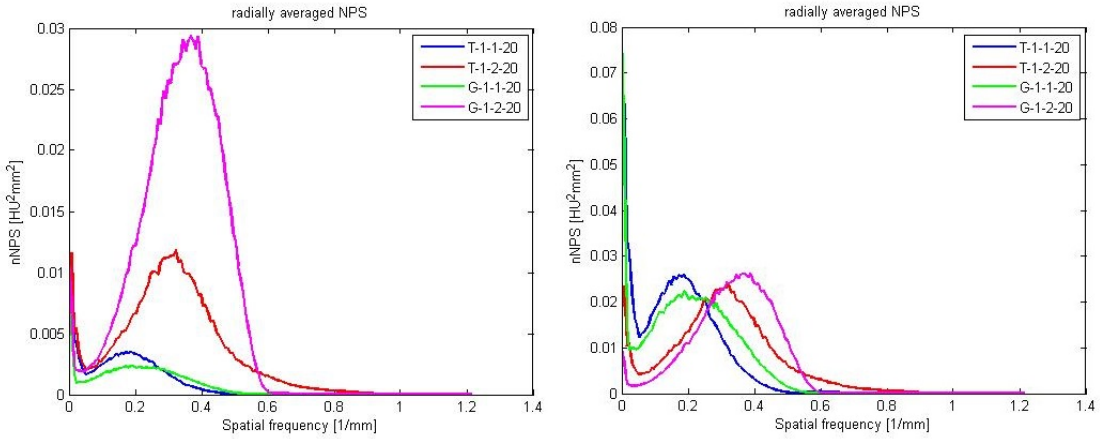


Figure 18: NPS for phantom without ring. Plot on the left presents NPS divided by area of ROI, while plot on the right, NPS divided by area under the curve. This way the inspection of the shape and peak location of the NPS can be spotted easier. However, it must be remembered that the magnitude information is lost there.

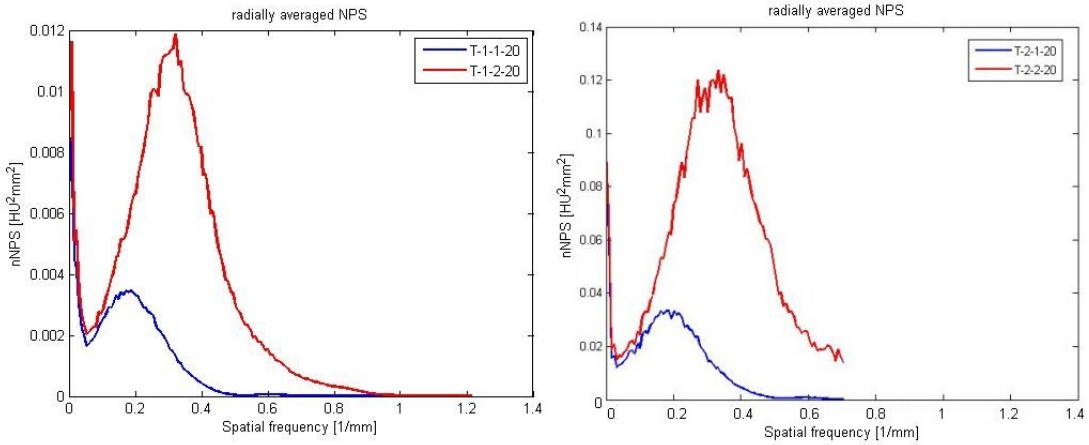


Figure 19: NPS of Toshiba protocols. Plot on the left presents NPS of Toshiba kernels without additional rings, on the right the first ring is introduced. Blue curve represents standard kernel, red the edge enhancing one.

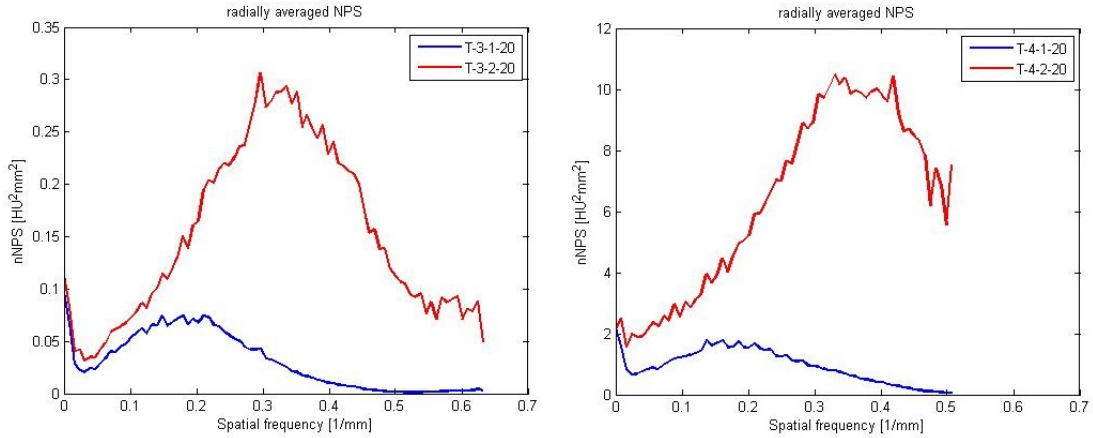


Figure 20: NPS of Toshiba protocols. Plot on the left presents NPS of Toshiba kernels with second ring, on the right the largest ring is introduced. Blue curve represents standard kernel, red the edge enhancing one.

more used scanner.

Figures: 21 and 22 present the comparison of filtered NPS between the scanners, for the maximum radiation dose(different doses are only scaled versions of these figures, so their curves are not analyzed here, but later in this chapter in different way). Also the additional group of datasets for Toshiba, where convolution kernel FC08 is used, is analyzed separately.

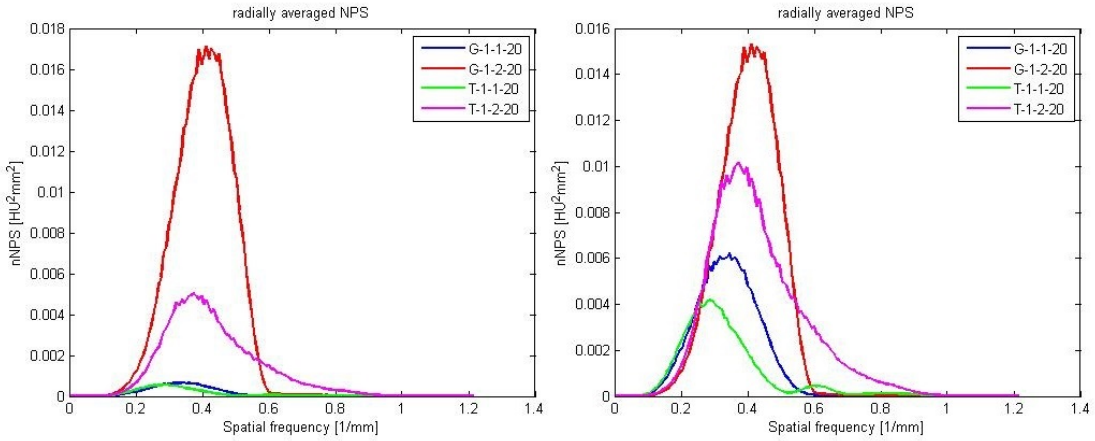


Figure 21: Filtered NPS for phantom without ring. GE kernels exhibits noise higher that their Toshiba counterparts. Plot on the left presents NPS divided by area of ROI, while plot on the right, NPS divided by area under the curve.

It is notable that GE standard kernel increases its performance in relation to Toshiba standard kernel, with increase of ring size (Figure 22). The difference is particularly noticeable for the largest ring, where GE clearly outperforms Toshiba, in both standard and sharp filter. Simplified comparison can be seen on Figure 23. For no ring introduced, Toshiba kernels have both lower

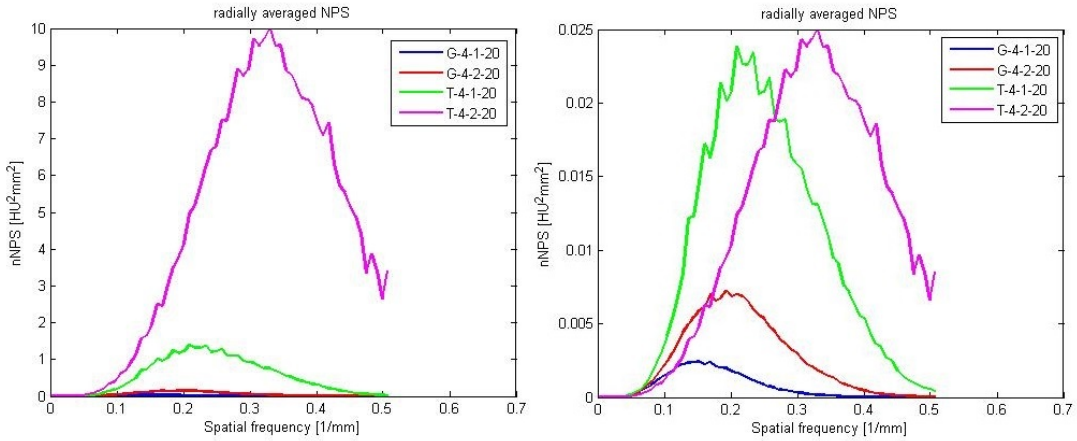


Figure 22: Filtered NPS for phantom with largest ring ring. GE kernels clearly outperform their Toshiba counterparts. Plot on the left presents NPS divided by area of the ROI, while plot on the right, NPS divided by the area under the curve.

| | peak value | peak frequency | | peak value | peak frequency | | peak value | peak frequency | | peak value | peak frequency |
|---|---|---|---|---|---|---|---|---|---|---|---|
| G-1-1 | 0.000661 | 0.35 | G-2-1 | 0.014 | 0.27 | G-3-1 | 0.023 | 0.27 | G-4-1 | 0.04 | 0.18 |
| T-1-1 | 0.000558 | 0.29 | T-2-1 | 0.018 | 0.26 | T-3-1 | 0.048 | 0.23 | T-4-1 | 1.40 | 0.22 |
| T-1-3 | 0.000542 | 0.29 | T-2-3 | 0.017 | 0.26 | T-3-3 | 0.044 | 0.23 | T-4-3 | 1.28 | 0.22 |
| G-1-2 | 0.017135 | 0.42 | G-2-2 | 0.235 | 0.35 | G-3-2 | 0.328 | 0.37 | G-4-2 | 0.15 | 0.20 |
| T-1-2 | 0.005006 | 0.38 | T-2-2 | 0.118 | 0.35 | T-3-2 | 0.292 | 0.34 | T-4-2 | 9.98 | 0.34 |

Figure 23: Comparison of peak value and frequency of different kernels with different rings.

NPS peaks and the frequency at which they manifest. This advantage decrease with addition of the rings, to the point where GE has much better results for the largest ring. If we assume that rings simulate the examination of real patient well, these result are in agreement with the reports of hospital practitioners, who considered images from Toshiba more difficult in diagnosis. However, the largest ring introduces huge amounts of noise, and exceeds the field of view of both scanners, introducing extreme conditions which makes drawing conclusions from this case questionable.

**Root Mean Square Difference**

As can be seen from the Figure 24, with increasing size of rings, the noise power spectra become less and less similar. The difference between GE and Toshiba edge enhancing protocols is much higher, than between standard kernels. In standard case, RMSD value remains low for all cases but largest ring. Both Toshiba TC08 and TC18 were compared with standard GE kernel, and interestingly, with increasing size of the rings, the FC08, kernel compensating for beam hardening effect, is slightly more similar to GE standard kernel. This suggests that GE protocol also accounts for beam hardening effects and is dealing well with larger patients. This plot also presents the RMSD between edge enhancing kernels, GE and Toshiba, marked with green color. The value of RMSD is slightly higher than for standard kernels comparison, but the pattern is similar. There is a small difference at second ring case, when the difference is actually smaller than in first ring case.

## 4.3 Comparison of two Toshiba standard convolution kernels.

The comparison of Toshiba standard protocols FC18 and FC08 (without and with compensationg for beam hardening effect, respectively) was done both without and with filtering the NPS with human visual response function. For comparison of uniformity data, Figure 25 shows that the mean values across the module are very similar, and only in case of the biggest ring, differences higher than 3 HU are present. The locations of highest and lowest values, as well as proportions, are kept relatively constant throughout all datasets.

The visual comparison of phantom images makes it impossible to observe the differences between the protocols, for no/small rings due to negligible differences, and for biggest ring, due to excessive noise. In examination of NPS, one can realize that the differences between the protocols are minimal. The magnitude increases with lower dose, and with bigger ring, but the NPS curves have very similar shape. The differences are negligibly small for small rings, thus only the comparison for largest ring has been presented, in the Figure 26. It can be seen that actually the FC08 noise is higher for low-frequencies, and becomes lower than FC18 for higher frequencies. They merge again, when they approach the Nyquist frequency.

More detailed analysis is done with filtered NPS, since the compensation of beam hardening effect has an aim of improving the visual quality of the image for the medical practitioner. The visual differences of the curves are unspottable after filtering, thus the numerical analysis is performed.

In Figure 23 it can be seen, that peak of NPS is slightly lower for the FC08 protocol, and this difference is growing with increasing size of the ring, promoting the FC08. On the other hand, location of the peak is exactly the same for both kernels. The increase of dissimilarity can be

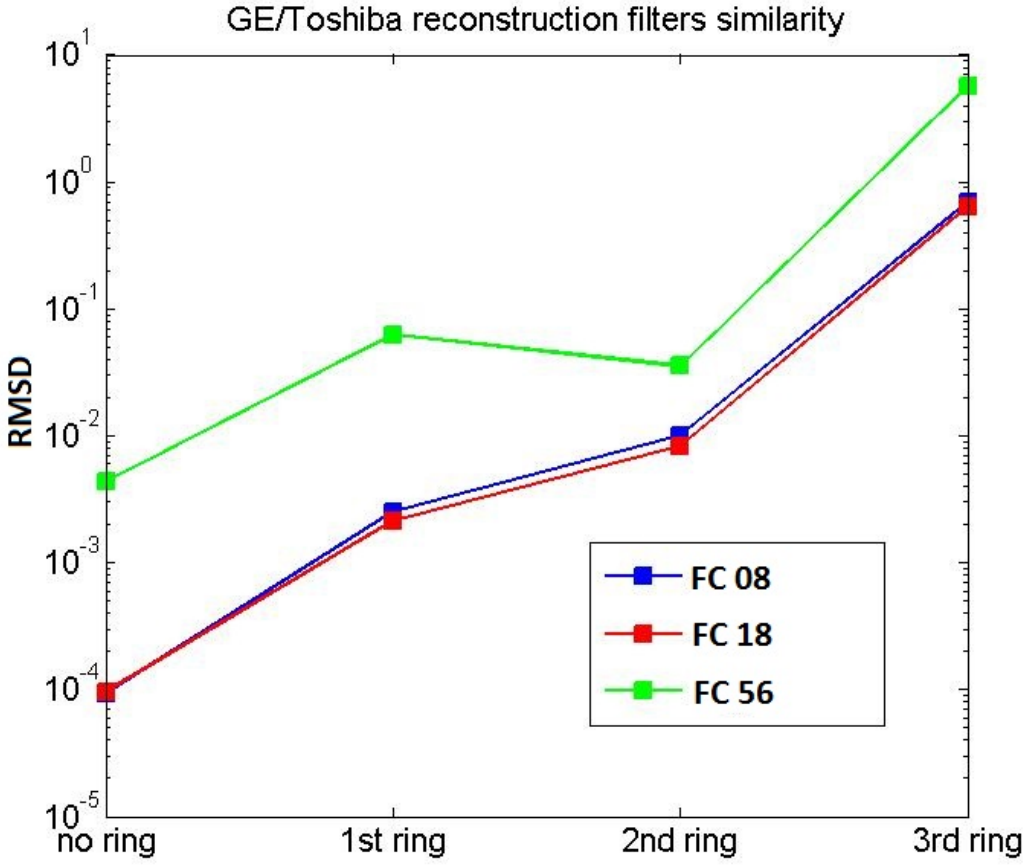


Figure 24: RMSD calculated for kernel pairs. GE standard kernel was compared with both Toshiba FC18 and FC08, to determine which is more similar, and decide on beam hardening compensation of GE standard kernel. GE and Toshiba edge enhancing kernels were compared with each other. Lower the value, the more similar the kernels are.

| dataset | ROI 1 | ROI 2 | ROI 3 | ROI 4 | ROI 5 | dataset | ROI 1 | ROI 2 | ROI 3 | ROI 4 | ROI 5 | difference | | | | |
|---|---|---|---|---|---|---|---|---|---|---|---|---|---|---|---|---|
| T-1-1-10 | 5.50 | 4.46 | 1.69 | 4.76 | 4.50 | T-1-3-10 | 4.33 | 3.30 | 0.56 | 3.58 | 3.32 | 1.18 | 1.16 | 1.12 | 1.18 | 1.18 |
| T-1-1-15 | 5.78 | 4.68 | 1.91 | 5.16 | 4.37 | T-1-3-15 | 4.58 | 3.51 | 0.78 | 3.98 | 3.22 | 1.20 | 1.16 | 1.13 | 1.18 | 1.16 |
| T-1-1-20 | 5.84 | 5.25 | 1.93 | 5.46 | 4.58 | T-1-3-20 | 4.65 | 4.08 | 0.82 | 4.26 | 3.41 | 1.19 | 1.16 | 1.11 | 1.20 | 1.17 |
| | | | | | | | | | | | | | | | | |
| T-2-1-10 | 8.67 | 6.31 | -0.71 | 6.10 | 5.73 | T-2-3-10 | 10.77 | 8.30 | 2.47 | 8.19 | 7.94 | 2.10 | 1.99 | 3.19 | 2.09 | 2.22 |
| T-2-1-15 | 8.67 | 5.24 | 0.42 | 5.81 | 6.87 | T-2-3-15 | 10.79 | 7.32 | 3.55 | 7.87 | 9.04 | 2.11 | 2.08 | 3.12 | 2.06 | 2.17 |
| T-2-1-20 | 7.54 | 6.13 | -0.26 | 6.47 | 6.42 | T-2-3-20 | 9.69 | 8.18 | 2.92 | 8.53 | 8.59 | 2.15 | 2.05 | 3.18 | 2.07 | 2.17 |
| | | | | | | | | | | | | | | | | |
| T-3-1-10 | 5.95 | 5.81 | 5.22 | 7.11 | 5.49 | T-3-3-10 | 7.52 | 6.95 | 6.37 | 8.14 | 6.62 | 1.57 | 1.13 | 1.15 | 1.04 | 1.12 |
| T-3-1-15 | 6.84 | 6.97 | 0.99 | 4.49 | 6.02 | T-3-3-15 | 8.45 | 7.99 | 2.30 | 5.66 | 7.11 | 1.61 | 1.02 | 1.32 | 1.17 | 1.09 |
| T-3-1-20 | 8.51 | 3.64 | 1.56 | 5.25 | 5.95 | T-3-3-20 | 10.17 | 4.83 | 2.83 | 6.35 | 7.02 | 1.67 | 1.19 | 1.27 | 1.10 | 1.07 |
| | | | | | | | | | | | | | | | | |
| T-4-1-10 | -104.70 | -68.14 | -123.67 | -70.43 | -68.48 | T-4-3-10 | -112.15 | -75.32 | -136.37 | -73.41 | -74.66 | 7.44 | 7.18 | 12.69 | 2.98 | 6.18 |
| T-4-1-15 | -76.83 | -46.65 | -74.35 | -33.54 | -40.03 | T-4-3-15 | -83.43 | -49.00 | -84.43 | -37.35 | -44.06 | 6.60 | 2.35 | 10.08 | 3.81 | 4.03 |
| T-4-1-20 | -63.91 | -28.77 | -57.39 | -25.48 | -32.79 | T-4-3-20 | -69.00 | -30.56 | -64.28 | -27.00 | -36.49 | 5.09 | 1.79 | 6.89 | 1.52 | 3.71 |

Figure 25: Mean CT numbers for Toshiba FC18 and FC08 kernels. Last panel shows the CT number difference between these two protocols for every ROI. Notice how constant this value is within the same ring

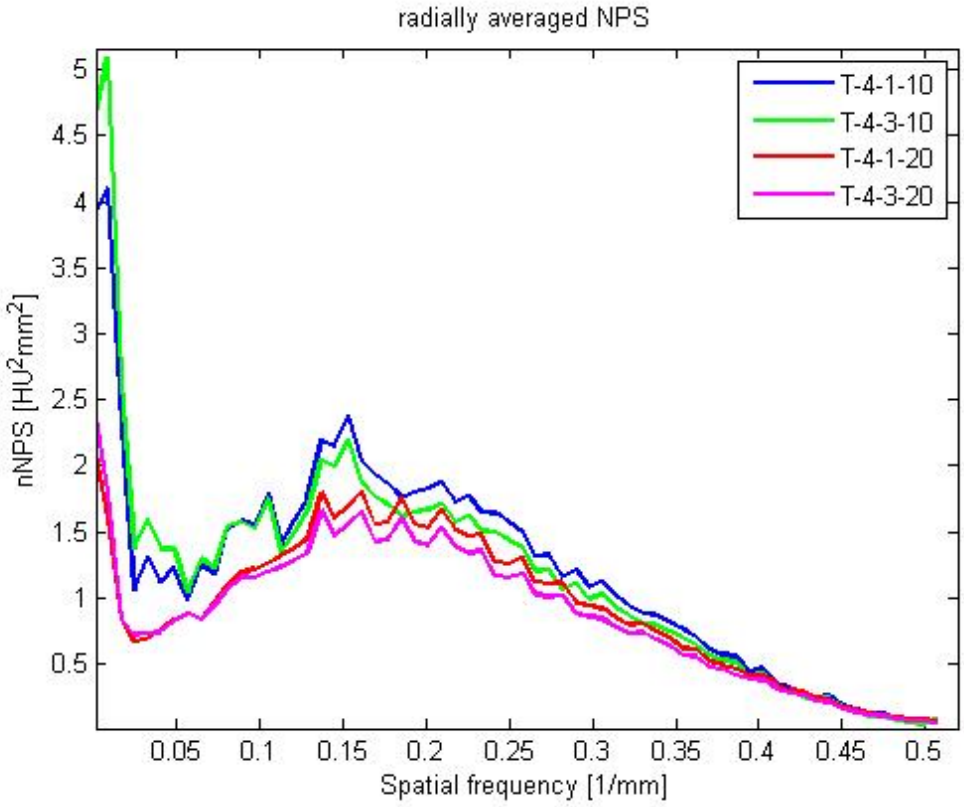


Figure 26: Plot of Toshiba standard kernels FC18 and FC08 for largest ring attached. Minimum and maximum doses are compared.

clearly seen in Figure 27, where the value of RMSD increases with the size of the rings.

This shows that the compensation for the beam hardening has some effect on the image, however, in the case of phantom uniformity module, it is not really perceivable, according to visual inspection of the images, and analysis of filtered NPS. The unfiltered NPS shows minimal differences, which further decrease with higher radiation dose. It is reasonable result, since with higher dose, smaller part of radiation get stopped, and beam hardening effect is lower.

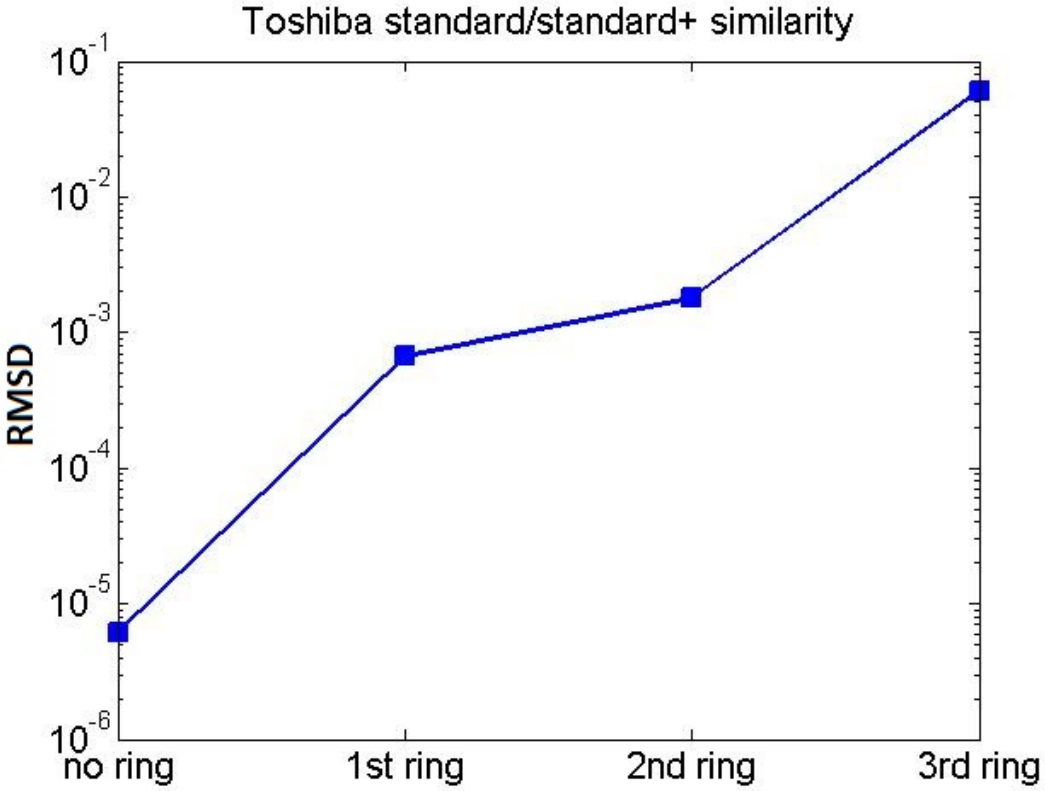


Figure 27: RMSD calculated for FC18 and FC08 Toshiba kernels.

## 4.4 Total Visible Noise ranking.

TVN results are the summary of all the NPS analysis and are plotted in Figure 28 in the form of a ranking, from best (lowest TVN) to worst (highest TVN). Due to their higher noise magnitude, the edge enhancing kernel datasets are at the end of all but one plot(largest ring). It is also visible that the FC08 datasets have lower TVN than FC18.

For the datasets without use of extension ring, Toshiba has lower TVN, so less noise visible for observer is present in the image. This is true for every case, because within the same kernel type and radiation dose, GE has worse results. With introduction of the first ring, GE datasets become the better than Toshiba within standard kernels comparison, and slightly improve but are still worse in edge enhancing cases. Situation further improves, but only slightly when second

ring is considered. Small difference between first and second ring datasets can be explained by small size difference and overall similarity of these two rings. Still, few GE datasets improved their position in the ranking. For the largest ring case, situation changes dramatically. Every dataset from GE scanner outperforms any of those from Toshiba, significantly. Even the datasets where edge enhancing kernel was used have much lower TVN than those of standard kernel from Toshiba. This clearly shows that GE handles scanning large objects better than Toshiba. However, the fact that improvement is so big, might be somehow related to the fact that largest ring has different shape than other rings.

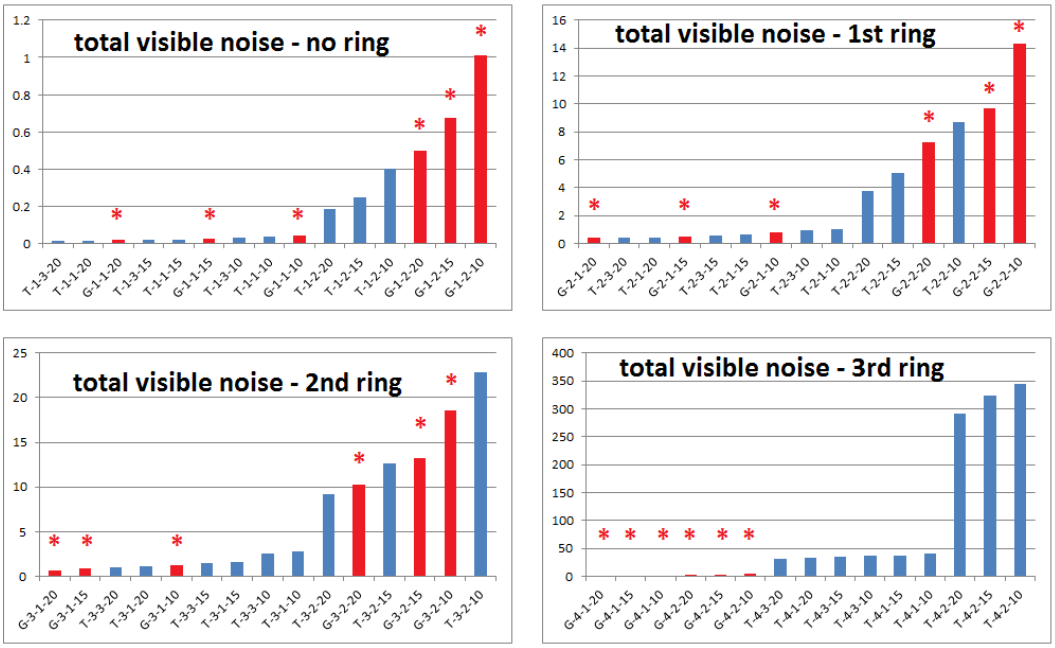


Figure 28: These plots show TVN values ordered in increasing order for all created datasets. Apart from names beneath, color coding was added, with blue for Toshiba datasets, and red for GE datasets. Additionally, red datasets are marked with a red star above them, for easier recognition from blue ones in the regions where the TVN values are small to the point of their bar not being visible. This also eases spotting the changes in the order with increase of the ring size.

# 5 Discussion

There are standard quality evaluation procedures in use for the phantom, but this is an ideal case. Rings simulate larger patients, where the information about organs, which are of interest, are beneath the layers of tissues that cause beam hardening effect and make the desired region of image disturbed with artifacts. Also, the extension rings used in this work are, up to this date, not been used in available literature. In that way, this work is a novelty in the field, and because of that, problems not encountered before were present.

In summary, all the results prove that introduction of ring significantly alters the image of the phantom. Without the rings, Toshiba scanner had much better performance in terms of image fidelity. However, the GE scanner handled addition of the rings much better than Toshiba, and performed significantly better, specially in the largest ring case. However, this ring had different shape than previous ones, and could not be entirely fitted into measurable FOV. Perhaps these are the reasons behind such dramatic difference in the performance for this ring. Nonetheless, for other rings the improvement of GE was a fact, and it had lower noise parameters for most of the datasets analyzed. This is an argument that supports the conclusion about GE superiority even if the largest, 'extreme case' ring results are discarded.

Another conclusion is related to two different kinds of the same convolution kernel of Toshiba confronted. The results for FC08 and FC18 were favoring FC08, which was the expected result, because with increasing size, more beam hardening effect would disrupt the image, and FC08 should control it in a better way than FC18. However, visual comparison showed no visible differences (and that was the reason this comparison was included into thesis, with no visual difference, the scientifically measurable difference was searched for), and even the detailed mathematical analysis indicated minimal influence of 'beam hardening compensation'. In the end, that is not something that would improve the quality of diagnostic data for the end user.

There are several more tests that could have been performed, and the conditions of the experiment could have been designed better. These flaws were the effect of low experience of the author, limited time and access to hospital equipment, and finally novel problems encountered for the first time in this field. Overall however, certain scientific progress was achieved which opens future possibilities of more detailed and better designed analysis and hopefully, more effective CT imaging.

# 6 Future work

It is not widely used to examine data from homogeneity module of a phantom, with addition of annuli. Thus, more complex analysis of such data would provide more complete scope of the effects on image quality, helping in protocol and dose selection for patients with not standard body mass.

There are several parameters that were not obtained due to limitations in time and access to CT scanners. The parameters giving more insight on the difference between systems, are signal-to-noise ratio, and Noise Equivalent Quanta. These would provide information on how efficiently the system is using the radiation dose to create the image, in other words, what fraction of the x-rays the patient is exposed to, contribute to the signal used in image reconstruction. Perhaps implementing these additional methods would reveal an observable difference between Toshiba protocols FC08 and FC18, which were compared, and no differences were found.

Bigger pixel matrix could provide an opportunity to select several ROIs from each slice, while still having reasonable size of ROI to contribute meaningfully to the NPS. It would be interesting to investigate in more depth the texture of images obtained. Several statistical methods could be employed, for example Gray-Level Co-occurrance Matrix, which open access to numerous parameters, that might give more information on the characteristics of the noise texture in CT images from different vendors

Another interesting approach would be analysis of Non-stochastic NPS (NPS of averaged slice), that was started but stopped, due to lack of time and no reference of use of such technique in any research related to CT. The analysis was designed, and the initial results that can be seen in Figure 29 were obtained. The interesting spatial patterns of 2D NPS that correspond to deterministic noise might be connected to the character of the scanner, and its working principles, perhaps giving answers to their performance when the rings were introduced.

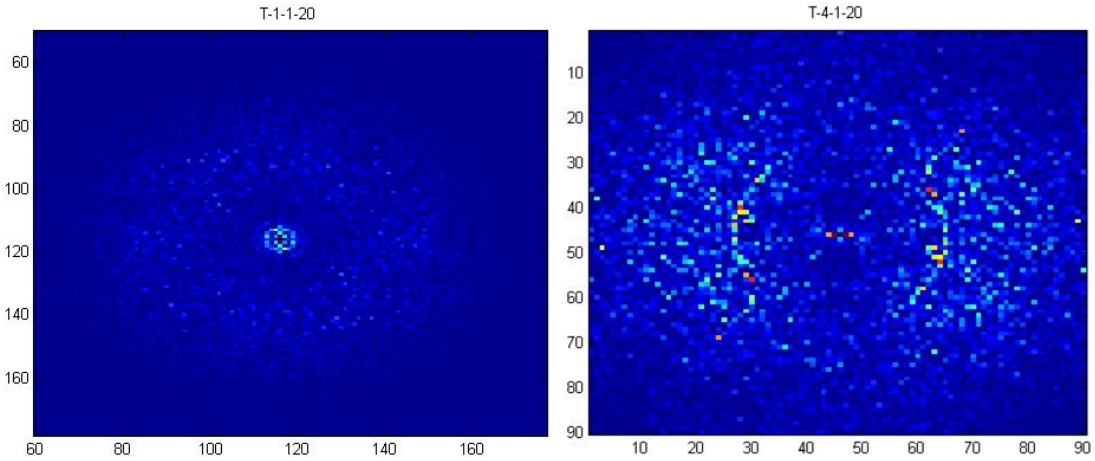


Figure 29: Both images present non-stochastic 2D NPS. In both cases, characteristic, circular patterns can be observed, that might be related to the performance of the scanner. It is also not certain that this kind of deterministic noise would be present in different scanner of the same type and vendor.

# Bibliography

[1] Kalender, W. A. 2000. *Computed Tomography*. Publicis MCD Vertag.

[2] Smith-Bindman, R., Lipson, J., & R. Marcus, e. a. 2009. Radiation dose associated with common computed tomography examinations and the associated lifetime attributable risk of cancer. *Archives of Internal Medicine*, 169(22), 2078–2086.

[3] Brenner, D. & Hall, E. 2007. Computed tomography - an increasing source of radiation exposure. *New England Journal of Medicine*, 357, 2277–84.

[4] Joemai, R. M. S., Geleijns, J., & Veldkamp, W. J. H. 2010. Development and validation of a low dose simulator for computed tomography. *European Radiology*, 20, 958–966.

[5] McCollough, C. H.; Leng, S. Y. L. C. D. D. B. J. M. M.-G. M. F. 2011. Ct dose index and patient dose: They are not the same thing. *Radiology*, 259, 311–316.

[6] Boas, F. E. & Fleischmann, D. 2012. Ct artifacts: Causes and reduction techniques. *Imaging Med.*, 4(2)(22), 229–240.

[7] Mansson, L. G. 2000. Methods for the evaluation of image quality: A review. *Radiation Protection Dosimetry*, 90, 89–99.

[8] Samei, E. & Flynn, M. J. 2003. An experimental comparison of detector performance for direct and indirect digital radiography systems. *Medical Physics*, 30, 608–622.

[9] Boedeker, K. L. & McNitt-Gray, M. F. 2007. Application of the noise power spectrum in modern diagnostic mdct: part ii. noise power spectra and signal to noise. *Physics in Medicine and Biology*, 52, 4047–4061.

[10] Faulkner, K. & Moores, B. M. 1984. Analysis of x-ray computed tomography images using the noise power spectrum and autocorrelation function. *Physics in Medicine and Biology*, 29, 1343–1352.

[11] Solomon, J. B., Christianson, O., & Samei, E. 2012. Quantitative comparison of noise texture across ct scanners from different manufacturers. *Medical Physics*, 39(10), 6048–6055.

[12] Armstrong, J. S. & Collopy, F. 1992. Error measures for generalizing about forecasting methods: Empirical comparisons. *International Journal of Forecasting*, 8, 69–80.

[13] ThePhantomLaboratory. May 2013. The phantom laboratory website. URL: `http://www.phantomlab.com/`.

[14] ThePhantomLaboratory. 2006. Catphan 500 and 600 phantom manual.

[15] Boedeker, K. L., Cooper, V. N., & McNittGray, M. F. 2007. Application of the noise power spectrum in modern diagnostic mdct: part i. measurement of noise power spectra and noise equivalent quanta. *Physics in Medicine and Biology*, 52, 4027–4046.

[16] Saunders, R., Jr., & Samei, E. 2006. Resolution and noise measurements of five crt and lcd medical displays. *Medical Physics*, 33, 308.

[17] McGill, R., Tukey, J. W., & Larsen, W. A. 1978. Variations of box plots. *The American Statistician*, 32, 12–16.

# A Appendix

This appendix contains sections of the brochure of Catphan Phantom 600 and manuals for the rings used. They all belong to the producer, The Phantom Laboratory.

# Catphan® 500/600

The Phantom Laboratory

# Catphan® 500/600

*Internationally recognized for measuring the* ***maximum*** *obtainable performance of axial, spiral and multi-slice CT scanners.*

## Extensive Research

The Phantom Laboratory *and physicist David Goodenough, Ph.D., have worked together to develop the Catphan® Phantoms. (Dr. Goodenough has been involved in CT performance testing since the first generation EMI Scanner.) The new Catphan® designs are based on over 25 years of scientific research and direct field experience in the evaluation of medical imaging equipment.* > >

## Convenient Set-Up

The Catphan® Phantom's patented design includes many exclusive features that make it easy to achieve perpendicular alignment. As all of the test sections are arranged at prescribed intervals from the first module, operators can quickly scan all test sections in a single sequence, eliminating the need to reposition the phantom for each section. In addition, the integral case mount allows the phantom to be positioned in the scanner, supported off the end of the table, eliminating table artifacts. The case is also equipped with a level to aid in positioning. Fast, easy positioning and the universal mount of the Catphan® Phantom makes it ideal for daily quality assurance programs on any scanner.

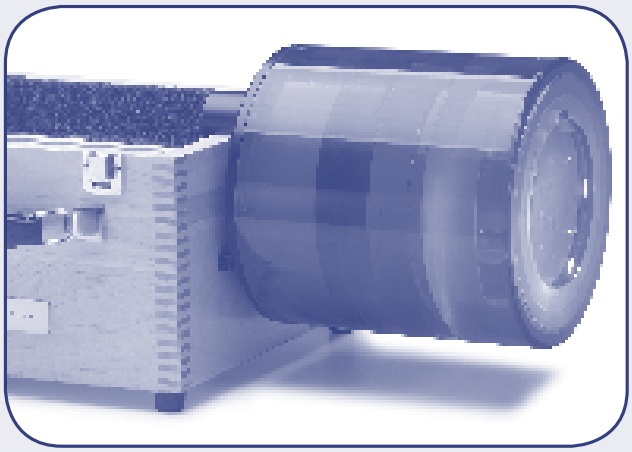

Fast, easy positioning and the universal mount of the Catphan® Phantom makes it ideal for daily quality assurance programs on any scanner.

## Solid-Cast Construction

Catphan® Phantoms are constructed from modules that fit snugly into a durable 20cm housing. Both the 500 and 600 Catphan® models are made from solid-cast materials, eliminating material absorption of water and leaks associated with water bath phantoms, as well as problems related to varied water sources.

## Modular Design

The Catphan® modular design allows test modules to be interchanged. As your testing needs change and new modules are developed, you can upgrade test modules that are compatible with your Catphan® system. Additionally, the modular design makes the Catphan® system ideal for traveling physicists and engineers who conduct comprehensive evaluations of CT scanners at multiple locations, as they are easily transportable and no draining is required between uses.

This brochure deals with two primary Catphan® models: the Catphan® 500 fifth generation model designed to address specific concerns associated with spiral CT scanners and the Catphan® 600 sixth generation model designed to evaluate the maximum performance potential of multi-slice CT Scanners.

## Catphan® 500

Designed to evaluate the maximum performance potential of axial and spiral CT scanners.

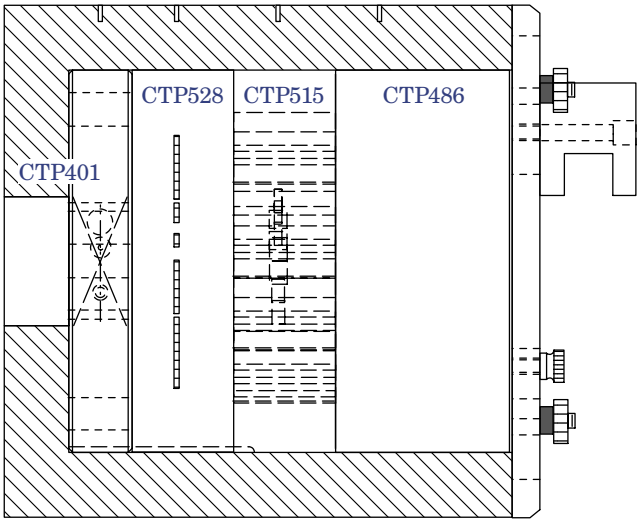


## Catphan® 600

Designed to evaluate the maximum performance potential of multi-slice CT scanners with enhanced sensitometry samples for radiation therapy planning.

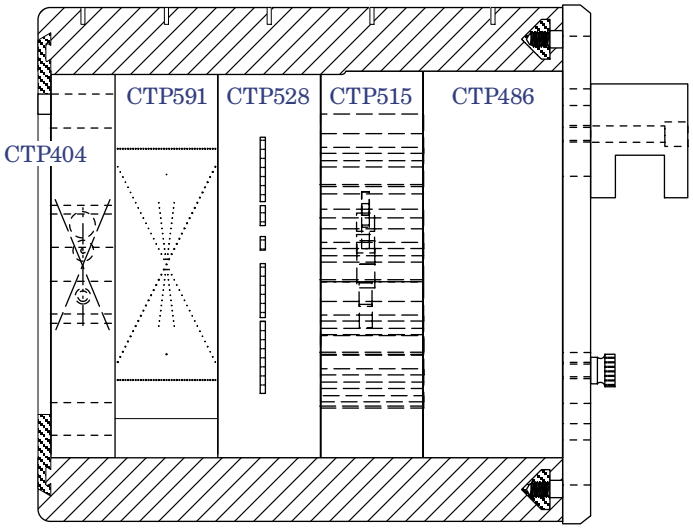


| Test Module | 500 | 600 |
|---|---|---|
| CTP401 module with slice width, pixel size and sensitometry (Teflon, Acrylic, LDPE, Air) | X | |
| CTP404 module with slice width, pixel size and sensitometry (Teflon, Delrin Acrylic, Polystyrene, $H_20$, LDPE, PMP, Air) | | X |
| CTP515 low contrast module with supra-slice and subslice contrast targets | X | X |
| CTP486 image uniformity module | X | X |
| CTP591 module with slice geometry and point source bead module | | X |

## Tests - Summary

- Scan slice geometry (slice width and slice sensitivity profile)*
- high resolution (1 to 21 line pairs per cm)
- phantom position verification
- patient alignment system check
- low contrast sensitivity
- comparative subslice and supra-slice low contrast sensitivity
- spatial uniformity
- scan incrementation
- noise (precision) of CT systems
- circular symmetry
- sensitometry (linearity)**
- pixel (matrix) size
- point spread function and modulation transfer function (MTF) for the x, y, and z axes*

* The CTP591 module contained in the Catphan® 600 described in this brochure enables these test measurements to be conducted in multiple slices covering a range of detector positions from a singlescan sequence. This eliminates the need to reposition the table and repeat scans to cover the z axis range of the multi-slice detectors.

* * The CTP404 module contained in the Catphan® 600 includes 3 additional sensitometry targets along with a small vial for a water sample. See the description for the CTP404 for more details.


## CTP486

### Uniformity Module

Diameter: 15cm | Thickness: >40mm

- spacial uniformity (noise)
- noise (precision) of CT systems

---

### Unique Advantages

The CTP486 does not leak and is not damaged by exposure to freezing temperatures because it does not use water. While water is generally considered the standard calibration material, many physicists prefer using our CTP486 solid-image uniformity module because it provides consistent results, is much more convenient to use than modules using water-filled tanks, and eliminates variations due to different water sources.

The CTP486 module is cast from a uniform material that has a CT number within 2% (0-20H) of water. This solid material's high radial and axial uniformity makes it an ideal substitute for water. It has been thoroughly tested over a wide variety of variables in the x, y and z planes and has proven stable in all applications.

---

## Also available from The Phantom Laboratory

The Phantom Laboratory is internationally recognized for producing dependable, high-precision phantoms for evaluating the performance of medical imaging and radiation therapy equipment.

**Magphan® Phantom**
Designed to perform a wide range of precision performance evaluations of Magnetic Resonance Imaging (MRI) Scanners.

**Specphan™ Phantom**
A New Test Tool For Single Photon Emission Computed Tomography (SPECT) and Coincidence Detection Systems.

**RANDO® Phantom**
Comprehensive verification of the complete treatment planning sequence.

**The RSVP Phantom™**
Provides stereotactic localization and dose verification for radiosurgery machines.

**The Phantom Patient™**
A full-body phantom with the dimensions of an average-size male patient, indispensable for training technicians in the use of radiography equipment.

**Sectional Phantoms**
Sectional Phantoms are ideal for training, calibration, and research.

**Liqui-Phil™ Phantoms**
Hollow phantoms that can be filled with liquid for nuclear medicine and MRI studies.

**Custom & OEM Phantoms**
Designed and manufactured to order.
Call for details.

The Phantom Laboratory is committed to the manufacture of high quality products. Our comprehensive quality system is registered in compliance with the internationally recognized ISO 9001:2000 standards.

## Contact Us

Please contact The Phantom Laboratory if you have any questions about our products.


**PHONE**:

518-692-1190 / 800-525-1190

**FAX:**

518-692-3329

**MAIL**:

The Phantom Laboratory, P.O. Box 511, Salem, NY 12865-0511 USA

**E-MAIL:**

General info: info@phantomlab.com

**Eileen Gerdes**, Manager –
Order Desk and Quality Systems:
gerdes@phantomlab.com

**Bonnie Hanlon**, Manager –
Production and Purchasing:
hanlon@phantomlab.com

**Joshua Levy**, President –
levy@phantomlab.com

**WEB:**

www.phantomlab.com

**part number**
CTP579



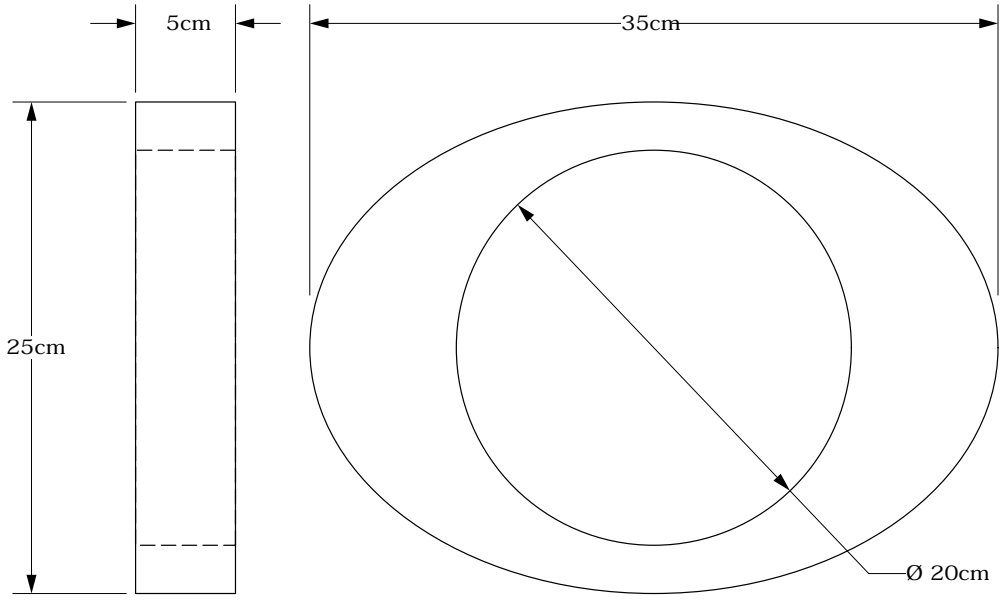


## 25-35cm OD Oval Body Annulus

The 25-35cm OD oval uniformity material body annulus creates varied attenuation for evaluation of image quality in a non-circular housing. This is ideal for assessing image quality with self-modulating low dose scanners.

The annulus is cast from the same material used in the Catphan® uniformity test module, CTP486. The Annulus fits over the 20cm housing of the Catphan® phantom.

The advantage of the oval annulus is it creates the varied attenuation which would be experienced in scanning a patient.

The Phantom Laboratory

**phone**
800-525-1190 or 518-692-1190
**fax**
518-692-3329

**mail**
P.O. Box 511
Salem, New York 12865
**shipping**
2727 State Route 29
Greenwich, New York 12834

**email**
info@phantomlab.com
**web**
www.phantomlab.com

**part number**
CTP599



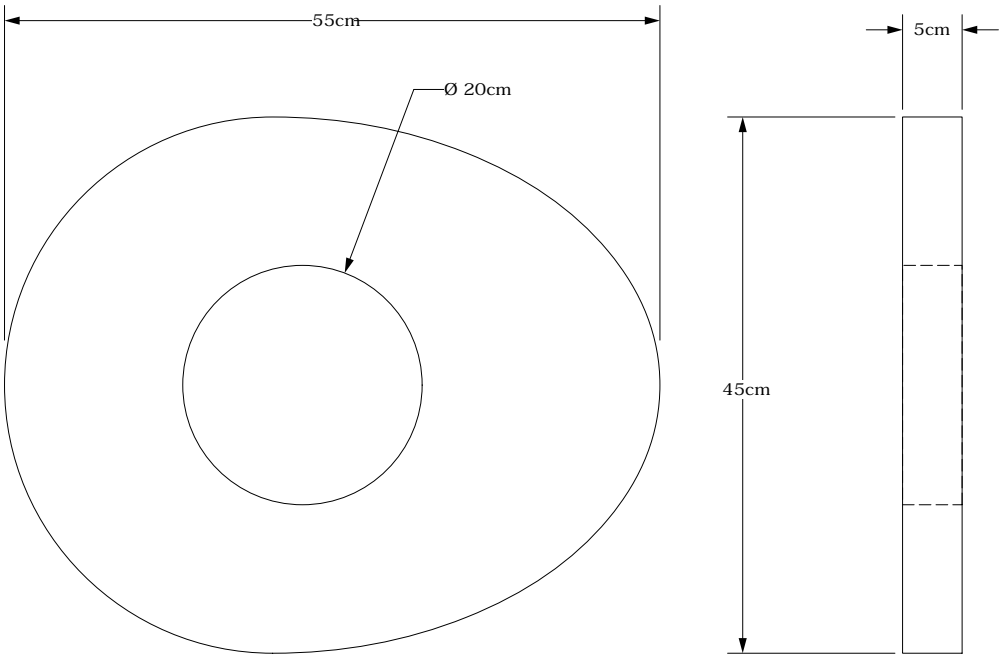


## 45-55cm Oval OD Uniformity Material Body Annulus, CTP599

The 45-55cm oval OD annulus can be slid over a 20cm Catphan® housing to mimic a very large body's imaging attenuation. The egg-shaped off-center annulus is cast from our uniformity material that is within 2% (0-20H) of water density.

The Phantom Laboratory

**phone**
800-525-1190 or 518-692-1190
**fax**
518-692-3329

**mail**
P.O. Box 511
Salem, New York 12865
**shipping**
2727 State Route 29
Greenwich, New York 12834

**email**
info@phantomlab.com
**web**
www.phantomlab.com

**part number**
CTP651



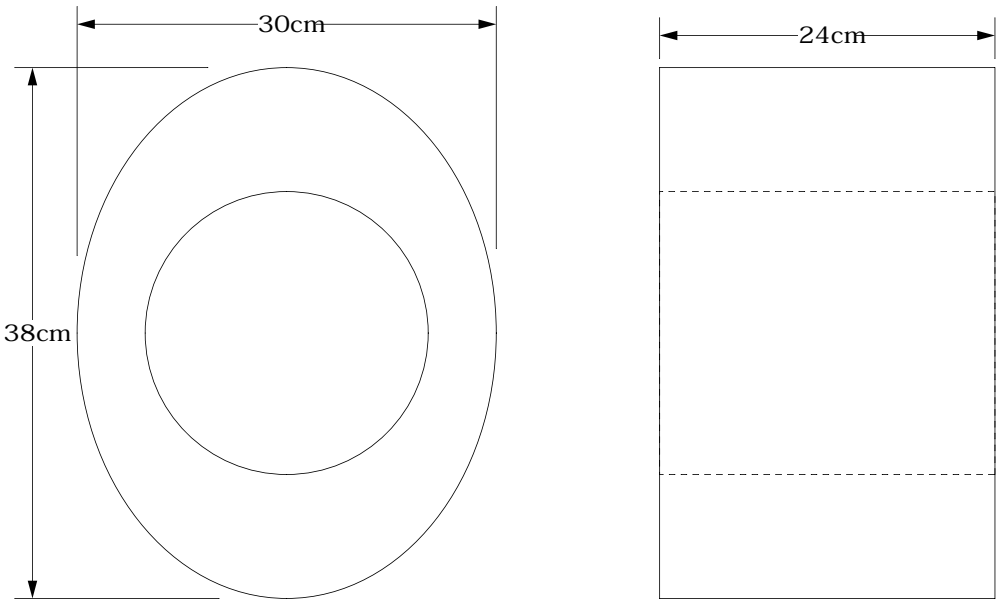


## 30-38cm OD Oval Body Annulus

The 30-38cm OD oval uniformity material body annulus creates varied attenuation for evaluation of image quality in a non-circular housing. This is ideal for assessing image quality with self-modulating low dose scanners.

The annulus is cast from the same material used in the Catphan® uniformity test module, CTP486. The Annulus fits over the 20cm housing of the Catphan® phantom.

The advantage of the oval annulus is it creates the varied attenuation which would be experienced in scanning a patient. This annulus can be manufactured in thickness ranging from 5cm to 24cm

**part number**
CTP600



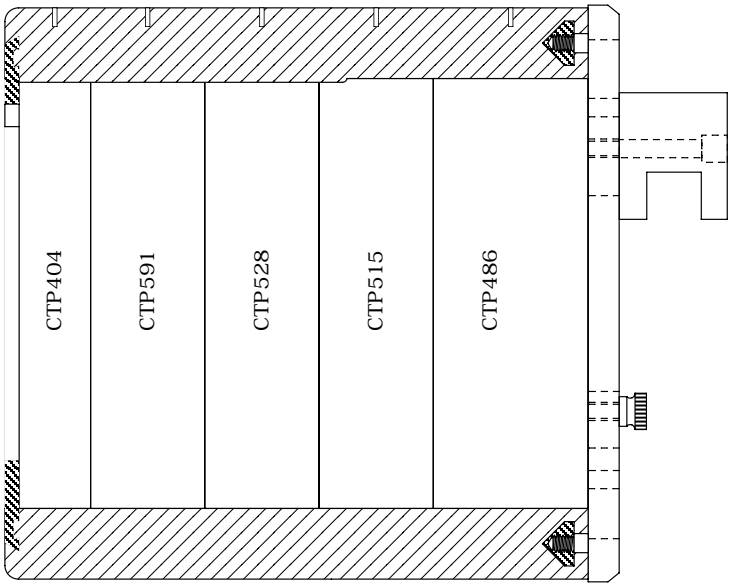


## Catphan® 600

The Catphan® 600 was designed to evaluate the maximum performance potential of multi-slice CT Scanners.

The Catphan® 600 combines the internationally recognized CTP528 and CTP515 modules contained in the Catphan® 500 with the versatility of the CTP591 slice geometry and point source bead module. The CTP591 bead module contains both course ramps (1mm z axis increments) and precision ramps (.25mm z axis increments) for evaluation of millimeter and sub-millimeter thin slices. Additionally the number of sensitometry samples has been increased.

Tests - Summary

- scan slice geometry (slice width and slice sensitivity profile)
  - slice width (wire ramps and bead ramps)
  - slice sensitivity profile (single slice or multiple slices)
  - x-y distance verification (50mm spaced rods)
- high resolution (up to 21 line pairs per cm)
- phantom position verification
- patient alignment system check
- low contrast sensitivity (40mm length solid cast targets)
- comparative subslice and supra-slice low contrast sensitivity
- spatial uniformity
- scan incrementation
- noise (precision) of CT systems
- circular symmetry
- sensitometry (linearity samples: air, PMP, LDPE, $H_2O$, Polystryene, Acrylic, Delrin, Teflon )
- pixel (matrix) size
- point spread function and modulation transfer function (MTF) for the x, y, and z axes

The Phantom Laboratory

**phone**
800-525-1190 or 518-692-1190
**fax**
518-692-3329

**mail**
P.O. Box 511
Salem, New York 12865
**shipping**
2727 State Route 29
Greenwich, New York 12834

**email**
info@phantomlab.com
**web**
www.phantomlab.com

# B Appendix

This appendix contains all results concerning the analysis of phantom uniformity. For all datasets, is lists the mean value(light red) and standard deviation(light yellow) for every region of interest. In addition, average mean and standard deviation for full dataset is given(blue).

| GE | | | mean | | | avr mean | | | std | | | avr std |
|---|---|---|---|---|---|---|---|---|---|---|---|---|
| dataset | ROI 1 | ROI 2 | ROI 3 | ROI 4 | ROI 5 | | ROI 1 | ROI 2 | ROI 3 | ROI 4 | ROI 5 | |
| G-1-1-10 | 12.41 | 11.45 | 11.86 | 11.88 | 11.61 | 11.84 | 5.60 | 5.51 | 6.11 | 5.81 | 5.62 | 5.73 |
| G-1-1-15 | 12.57 | 11.67 | 11.16 | 11.61 | 11.51 | 11.71 | 4.66 | 4.46 | 4.92 | 4.53 | 4.42 | 4.60 |
| G-1-1-20 | 12.53 | 11.92 | 11.10 | 11.81 | 11.63 | 11.80 | 3.61 | 3.72 | 4.22 | 3.97 | 3.85 | 3.87 |
| G-1-2-10 | 14.26 | 12.78 | 13.34 | 13.80 | 13.15 | 13.47 | 22.74 | 22.44 | 25.91 | 23.21 | 23.61 | 23.58 |
| G-1-2-15 | 14.20 | 13.29 | 12.67 | 13.54 | 12.86 | 13.31 | 17.21 | 17.80 | 20.44 | 18.07 | 18.80 | 18.46 |
| G-1-2-20 | 14.32 | 13.73 | 12.28 | 13.64 | 13.32 | 13.46 | 14.54 | 15.45 | 18.17 | 15.80 | 15.54 | 15.90 |
| G-2-1-10 | 10.28 | 0.12 | -4.62 | -1.08 | 5.80 | 2.10 | 13.63 | 17.11 | 16.88 | 17.16 | 14.19 | 15.79 |
| G-2-1-15 | 11.41 | -0.29 | -4.59 | -0.06 | 5.39 | 2.37 | 11.99 | 13.47 | 14.45 | 14.23 | 11.86 | 13.20 |
| G-2-1-20 | 10.57 | 0.61 | -3.98 | -0.55 | 5.27 | 2.38 | 9.65 | 12.64 | 12.82 | 12.74 | 9.69 | 11.51 |
| G-2-2-10 | 11.42 | 0.91 | -0.91 | -0.12 | 7.70 | 3.80 | 53.17 | 69.08 | 74.04 | 70.92 | 56.96 | 64.83 |
| G-2-2-15 | 12.80 | 0.39 | -0.45 | 1.26 | 6.30 | 4.06 | 46.40 | 55.75 | 63.55 | 58.89 | 46.08 | 54.13 |
| G-2-2-20 | 11.66 | 2.35 | -0.92 | 0.04 | 6.25 | 3.88 | 38.51 | 49.16 | 52.56 | 48.95 | 38.72 | 45.58 |
| G-3-1-10 | 2.00 | -6.94 | -14.84 | -8.37 | -0.98 | -5.82 | 18.09 | 20.34 | 19.00 | 19.02 | 17.74 | 18.84 |
| G-3-1-15 | 2.49 | -7.22 | -13.54 | -7.74 | -2.45 | -5.69 | 14.76 | 16.78 | 17.08 | 16.44 | 15.05 | 16.02 |
| G-3-1-20 | 1.69 | -7.47 | -15.29 | -8.50 | -3.03 | -6.52 | 13.80 | 15.07 | 16.91 | 14.38 | 13.45 | 14.72 |
| G-3-2-10 | 1.35 | -6.38 | -11.89 | -6.65 | 1.44 | -4.42 | 63.55 | 71.74 | 74.95 | 69.37 | 65.32 | 68.99 |
| G-3-2-15 | 2.94 | -5.90 | -12.24 | -6.43 | -1.42 | -4.61 | 53.42 | 60.47 | 67.14 | 60.46 | 56.20 | 59.54 |
| G-3-2-20 | 2.39 | -6.75 | -15.52 | -7.80 | -2.34 | -6.01 | 51.42 | 55.15 | 61.81 | 53.02 | 48.65 | 54.01 |
| G-4-1-10 | -84.80 | -76.32 | -90.07 | -84.59 | -74.23 | -82.00 | 22.07 | 20.39 | 19.80 | 18.61 | 19.85 | 20.14 |
| G-4-1-15 | -83.69 | -74.58 | -85.79 | -87.58 | -74.64 | -81.26 | 20.94 | 18.29 | 20.06 | 18.98 | 14.93 | 18.64 |
| G-4-1-20 | -79.01 | -74.49 | -85.89 | -88.40 | -74.53 | -80.46 | 16.76 | 19.88 | 20.32 | 15.62 | 17.99 | 18.11 |
| G-4-2-10 | -85.22 | -76.02 | -92.05 | -83.41 | -72.59 | -81.86 | 36.90 | 37.48 | 34.20 | 33.67 | 38.21 | 36.09 |
| G-4-2-15 | -82.67 | -73.37 | -86.44 | -85.83 | -73.55 | -80.37 | 35.23 | 34.40 | 32.39 | 33.41 | 27.18 | 32.52 |
| G-4-2-20 | -77.95 | -73.59 | -87.38 | -87.96 | -73.27 | -80.03 | 28.89 | 33.09 | 33.01 | 28.73 | 31.35 | 31.02 |

| TOSHIBA | | | mean | | | avr mean | | | std | | | avr std |
|---|---|---|---|---|---|---|---|---|---|---|---|---|
| dataset | ROI 1 | ROI 2 | ROI 3 | ROI 4 | ROI 5 | | ROI 1 | ROI 2 | ROI 3 | ROI 4 | ROI 5 | |
| T-1-1-10 | 5.50 | 4.46 | 1.69 | 4.76 | 4.50 | 4.18 | 6.34 | 5.98 | 6.55 | 6.21 | 6.05 | 6.23 |
| T-1-1-15 | 5.78 | 4.68 | 1.91 | 5.16 | 4.37 | 4.38 | 4.72 | 4.36 | 5.83 | 4.69 | 4.83 | 4.89 |
| T-1-1-20 | 5.84 | 5.25 | 1.93 | 5.46 | 4.58 | 4.61 | 4.04 | 4.15 | 4.99 | 4.02 | 4.07 | 4.25 |
| T-1-2-10 | 6.62 | 5.63 | 1.44 | 5.57 | 5.25 | 4.90 | 15.81 | 14.96 | 16.31 | 15.48 | 14.89 | 15.49 |
| T-1-2-15 | 6.56 | 5.47 | 1.44 | 6.29 | 5.21 | 4.99 | 12.62 | 11.18 | 13.48 | 11.92 | 12.33 | 12.31 |
| T-1-2-20 | 6.78 | 6.03 | 1.82 | 6.29 | 5.56 | 5.29 | 10.48 | 10.21 | 11.90 | 10.27 | 10.50 | 10.67 |
| T-2-1-10 | 8.67 | 6.31 | -0.71 | 6.10 | 5.73 | 5.22 | 17.10 | 21.21 | 19.69 | 20.51 | 17.40 | 19.18 |
| T-2-1-15 | 8.67 | 5.24 | 0.42 | 5.81 | 6.87 | 5.40 | 13.26 | 15.92 | 15.98 | 16.92 | 13.47 | 15.11 |
| T-2-1-20 | 7.54 | 6.13 | -0.26 | 6.47 | 6.42 | 5.26 | 11.10 | 14.21 | 12.35 | 12.75 | 12.03 | 12.49 |
| T-2-2-10 | 8.53 | 7.41 | -0.48 | 6.99 | 5.40 | 5.57 | 45.92 | 56.36 | 55.00 | 54.37 | 46.05 | 51.54 |
| T-2-2-15 | 9.31 | 5.16 | 1.00 | 6.69 | 7.42 | 5.91 | 34.00 | 44.18 | 44.18 | 42.49 | 36.17 | 40.21 |
| T-2-2-20 | 7.99 | 6.34 | -0.63 | 6.65 | 6.89 | 5.45 | 30.04 | 36.45 | 35.29 | 35.41 | 31.32 | 33.70 |
| T-3-1-10 | 5.95 | 5.81 | 5.22 | 7.11 | 5.49 | 5.92 | 27.57 | 29.63 | 32.16 | 31.28 | 25.32 | 29.19 |
| T-3-1-15 | 6.84 | 6.97 | 0.99 | 4.49 | 6.02 | 5.06 | 20.84 | 22.21 | 22.52 | 23.33 | 19.90 | 21.76 |
| T-3-1-20 | 8.51 | 3.64 | 1.56 | 5.25 | 5.95 | 4.98 | 18.83 | 18.43 | 18.15 | 20.12 | 17.08 | 18.52 |
| T-3-2-10 | 4.01 | 6.92 | 4.85 | 8.13 | 5.37 | 5.86 | 74.38 | 82.00 | 83.85 | 87.21 | 67.66 | 79.02 |
| T-3-2-15 | 6.99 | 7.57 | 1.78 | 5.30 | 6.35 | 5.60 | 56.79 | 59.75 | 61.68 | 60.36 | 53.03 | 58.32 |
| T-3-2-20 | 9.02 | 4.27 | 2.21 | 5.07 | 6.21 | 5.36 | 48.29 | 52.14 | 48.41 | 54.38 | 44.04 | 49.45 |
| T-4-1-10 | -104.70 | -68.14 | -123.67 | -70.43 | -68.48 | -87.09 | 97.51 | 103.06 | 130.51 | 100.65 | 99.80 | 106.31 |
| T-4-1-15 | -76.83 | -46.65 | -74.35 | -33.54 | -40.03 | -54.28 | 91.82 | 96.20 | 115.54 | 101.16 | 101.38 | 101.22 |
| T-4-1-20 | -63.91 | -28.77 | -57.39 | -25.48 | -32.79 | -41.67 | 92.66 | 89.46 | 102.50 | 96.00 | 91.59 | 94.44 |
| T-4-2-10 | -108.22 | -65.50 | -129.07 | -62.03 | -78.41 | -88.65 | 260.79 | 265.03 | 306.37 | 266.32 | 270.25 | 273.75 |
| T-4-2-15 | -77.35 | -47.62 | -70.70 | -36.34 | -37.24 | -53.85 | 269.49 | 256.49 | 274.82 | 279.28 | 266.07 | 269.23 |
| T-4-2-20 | -54.30 | -42.48 | -62.03 | -20.39 | -33.44 | -42.53 | 242.18 | 240.79 | 256.03 | 262.70 | 252.85 | 250.91 |

| TOSHIBA | | | mean | | | avr mean | | | std | | | avr std |
|---|---|---|---|---|---|---|---|---|---|---|---|---|
| dataset | | | | | | | | | | | | |
| T-1-3-10 | 4.33 | 3.30 | 0.56 | 3.58 | 3.32 | 3.02 | 6.25 | 5.89 | 6.45 | 6.11 | 5.95 | 6.13 |
| T-1-3-15 | 4.58 | 3.51 | 0.78 | 3.98 | 3.22 | 3.21 | 4.64 | 4.31 | 5.75 | 4.62 | 4.76 | 4.82 |
| T-1-3-20 | 4.65 | 4.08 | 0.82 | 4.26 | 3.41 | 3.44 | 3.97 | 4.09 | 4.91 | 3.95 | 3.99 | 4.18 |
| | | | | | | | | | | | | |
| T-2-3-10 | 10.77 | 8.30 | 2.47 | 8.19 | 7.94 | 7.53 | 16.34 | 20.29 | 18.75 | 19.59 | 16.69 | 18.33 |
| T-2-3-15 | 10.79 | 7.32 | 3.55 | 7.87 | 9.04 | 7.71 | 12.66 | 15.24 | 15.30 | 16.19 | 12.88 | 14.46 |
| T-2-3-20 | 9.69 | 8.18 | 2.92 | 8.53 | 8.59 | 7.58 | 10.61 | 13.62 | 11.80 | 12.16 | 11.48 | 11.93 |
| | | | | | | | | | | | | |
| T-3-3-10 | 7.52 | 6.95 | 6.37 | 8.14 | 6.62 | 7.12 | 26.32 | 28.34 | 30.54 | 29.92 | 24.21 | 27.87 |
| T-3-3-15 | 8.45 | 7.99 | 2.30 | 5.66 | 7.11 | 6.30 | 19.94 | 21.24 | 21.55 | 22.32 | 19.05 | 20.82 |
| T-3-3-20 | 10.17 | 4.83 | 2.83 | 6.35 | 7.02 | 6.24 | 18.06 | 17.63 | 17.35 | 19.26 | 16.36 | 17.73 |
| | | | | | | | | | | | | |
| T-4-3-10 | -112.15 | -75.32 | -136.37 | -73.41 | -74.66 | -94.38 | 94.22 | 98.77 | 130.41 | 96.69 | 96.29 | 103.28 |
| T-4-3-15 | -83.43 | -49.00 | -84.43 | -37.35 | -44.06 | -59.65 | 88.61 | 91.64 | 112.89 | 96.84 | 97.44 | 97.49 |
| T-4-3-20 | -69.00 | -30.56 | -64.28 | -27.00 | -36.49 | -45.47 | 89.51 | 85.76 | 99.39 | 91.96 | 88.18 | 90.96 |